Journal of Computational Physics 229 (2010) 788–812

Contents lists available at ScienceDirect

Journal of Computational Physics

journal homepage: www.elsevier.com/locate/jcp

Multi-dimensional limiting process for hyperbolic conservation laws on unstructured grids

Jin Seok Park [a], Sung-Hwan Yoon [a], Chongam Kim [a,b,*]

[a] School of Mechanical and Aerospace Engineering, Seoul National University, Seoul 151-742, Republic of Korea
[b] Institute of Advanced Aerospace Technology, School of Mechanical and Aerospace Engineering, Seoul National University, Seoul, Republic of Korea

ARTICLE INFO

Article history:
Received 28 January 2009
Received in revised form 6 October 2009
Accepted 7 October 2009
Available online 21 October 2009

Keywords:
Multi-dimensional limiting process
Multi-dimensional limiting condition
Unstructured grids
Slope limiters
Compressible flow

ABSTRACT

The present paper deals with an efficient and accurate limiting strategy for the multi-dimensional hyperbolic conservation laws on unstructured grids. The multi-dimensional limiting process (MLP) which has been successfully proposed on structured grids is extended to unstructured grids. The basic idea of the proposed limiting strategy is to control the distribution of both cell-centered and cell-vertex physical properties to mimic multi-dimensional nature of flow physics, which can be formulated to satisfy so called the MLP condition. The MLP condition can guarantee high-order spatial accuracy and improved convergence without yielding spurious oscillations. Starting from the MUSCL-type reconstruction on unstructured grids followed by the efficient implementation of the MLP condition, MLP slope limiters on unstructured meshes are obtained.

Thanks to its superior limiting strategy and maximum principle satisfying characteristics, the newly developed MLP on unstructured grids is quite effective in controlling numerical oscillations as well as accurate in capturing multi-dimensional flow features. Numerous test cases are presented to validate the basic features of the proposed approach.

1. Introduction

Recently, dramatic improvement of computing power and numerical method makes it feasible to analyze very large scale problems including complex flow structure around complete aircraft or rotorcraft [1,2]. As a result, CFD community is more and more concerned about flow physics around realistic aerodynamic configurations in multiple dimensions. Since manual production of grid system around multi-dimensional intricate configuration is a highly laboring task, various grid generation methodologies such as multi-block grids [3] or overset grids [4] have been developed. Difficulties in generating structured grids for complex geometries have also prompted intensive research and development in unstructured grid methods, which exhibit quite flexible and robust tessellation capability [5–7].

Aside from automatic and fast grid generation, a robust high-resolution scheme is also essential to solve large scale problems accurately and efficiently. With a higher-order accurate reconstruction scheme, it is possible to capture complex flow structures with an adequate number of grid points [8], which is especially conspicuous for flows including vortex-like structure. At the same time, it entails non-physical oscillations near discontinuities such as shock waves. Spurious oscillations may lead to wrong solution as well as serious convergence problem. Therefore, a robust and accurate oscillation control strategy should be incorporated into a higher-order interpolation scheme.

* Corresponding author. Tel.: +82 2 880 1915; fax: +82 2 887 2662. Address: School of Mechanical and Aerospace Engineering, Seoul National University, Seoul 151-742, Republic of Korea.
E-mail address: chongam@snu.ac.kr (C. Kim).

0021-9991/$ - see front matter © 2009 Elsevier Inc. All rights reserved.
doi:10.1016/j.jcp.2009.10.011

Many methods to control numerical oscillation have been explored, and several limiting concepts have been proposed. Most remarkable progresses would be TVD [9,10], TVB [11] and ENO [12]/WENO [13]. As successive studies, MP limiter [14] and ENO/WENO filters [15,16] have also been developed. Nevertheless, philosophies of most oscillation control methods are mainly based on one-dimensional convection equation, and it is often insufficient or almost impossible to control oscillations near physical discontinuities in multi-dimensional flow situations. This problem is mainly attributed to the difficulty of defining monotonicity in multiple dimensions. While the TVD criterion provides the fundamental framework to ensure monotonicity in one dimension, it does not provide equivalent performance in multiple dimensions [17]. Moreover, defining the monotonic distribution near saddle point is ambiguous. Thus, an alternative but implementable condition to ensure multi-dimensional monotonicity is required.

Reconstruction procedure on unstructured grids imposes additional difficulty. Interpolation on unstructured grids is not readily derived by difference formula due to random indexing, which increases the level of complexity. Following the MUSCL-type or LED framework, reconstruction methods were mainly focused on the calculation of solution gradient, within a cell or along an edge, which is needed for second-order accuracy [18–22]. In particular, Barth and Japerson proposed a single multi-dimensional slope limiting by extending Spekreijse's monotonic concept [20,23]. As successive studies, various refined limiters have been devised [24–26]. Furthermore, the MUSCL-type framework was also extended to k-exact reconstruction by introducing Hessian matrix [27] or ENO/WENO reconstruction [28,29]. From this perspective, higher-order methods, such as discontinuous Galerkin method (DG) [30], spectral volume method (SV) [31] and spectral difference method (SD) [32], have been actively studied in recent years.

Although current reconstruction methods have enjoyed successes in many applications, the optimal limiting strategy to fulfill a high-level of accuracy, robustness and convergence is still one of the main issues to be addressed. For example, some of the reconstruction methods are not successful in dealing with oscillations in multiple dimensions. This manifests the need to explore an effective limiting criterion and accurate oscillation control method for multi-dimensional computations.

In order to find out a suitable criterion for oscillation control in multiple dimensions, the one-dimensional monotonic condition was extended to multi-dimensional flows, and the multi-dimensional limiting process (MLP) was successfully formulated on structured grids [33,34]. From the series of studies, it has been clearly demonstrated that the MLP limiting strategy possesses favorable characteristics, such as accuracy and convergence enhancement in inviscid and viscous computations. Furthermore, the MLP limiting strategy can be implemented regardless of grid topology. In the present paper, a new robust and accurate limiting strategy on unstructured grids is proposed within the MUSCL-type framework.

This paper is organized as follows. At first, the MUSCL-type reconstruction is briefly described in Section 2. Then, the MLP on structured grids is summarized and the unstructured version of MLP is formulated in Section 3. In Section 4, various numerical test cases are carried out to verify the performance of the present method. Finally, conclusion is drawn in Section 5.

2. MUSCL-type finite volume methods on unstructured grids

2.1. MUSCL-type reconstruction

Let us consider the multi-dimensional hyperbolic conservation laws as follows.

$$\frac{\partial \mathbf{Q}}{\partial t} + \nabla \cdot \mathbf{F} = 0, \tag{1}$$

where $\mathbf{Q}$ is the state variable vector and $\mathbf{F}$ is the flux function vector. In finite volume method, Eq. (1) is integrated on the control volume T_j,

$$\int_{T_j} \frac{\partial \mathbf{Q}}{\partial t}\, dV + \int_{\partial T_j} \mathbf{F} \cdot \mathbf{n}\, dS = 0, \tag{2}$$

where $\mathbf{n}$ is an outward normal vector. Depending on the location of physical variables, one may use either a cell-centered or a cell-vertex approach. A cell-centered approach is adopted in the present work, but the same concept can be similarly implemented into a cell-vertex discretization.

After approximating the flux function numerically, the semi-discrete form of Eq. (2) can be written as follows.

$$|T_j| \frac{\partial \overline{\mathbf{Q}}_j}{\partial t} + \sum_{e_{jk} \in T_j} \mathbf{H}(\overline{\mathbf{Q}}_{jk}, \overline{\mathbf{Q}}_{kj}) |e_{jk}| = 0, \tag{3}$$

where $\bar{\mathbf{Q}}_j$ denotes the cell-averaged state vector, $\bar{\mathbf{Q}}_{jk}$ is the cell interface state vector of the direction from the cell T_j to the cell T_k. $|T_j|$ is the area of the cell T_j. e_{jk} denotes the edge between T_j and T_k, and $|e_{jk}|$ is its length. $\mathbf{H}(\mathbf{Q}_L, \mathbf{Q}_R)$ is the vector of a numerical flux function. Midpoint rule is applied to calculate the numerical flux.

Gradient in a cell is estimated by the MUSCL-type reconstruction. Employing a linear or quadratic distribution in a cell, a second-order or third-order accurate solution can be obtained, respectively. Since the present work is the starting point of developing an unstructured version of MLP, a linear distribution is assumed in a cell.

Similar to the one-dimensional MUSCL approach, reconstructed values are controlled by a limiter function to ensure monotonicity. For each component of the state variable vector, the limited reconstruction within a cell is expressed as follows.

$$q_j(x,y) = \bar{q}_j + \phi \nabla \bar{q}_j \cdot \mathbf{r}, \tag{4}$$

where q_j is the component of the state variable vector $\mathbf{Q}$, $\nabla \bar{q}_j$ is the estimated gradient of the cell T_j and ϕ is a limiting function. $\mathbf{r}$ is the vector from centroid of the cell T_j. Reconstruction becomes conservative if the integration of q_j over a cell equals the cell-averaged value.

$$\bar{q}_j = \frac{1}{|T_j|} \int_{T_j} q_j \, dV. \tag{5}$$

The cell interface values ($\mathbf{Q}_L$, $\mathbf{Q}_R$) are then calculated by Eq. (4).

Several methods have been proposed to approximate the linear gradient $\nabla \bar{q}_j$ and the limiting function ϕ [35]. Since the primary goal of the present work is to control numerical oscillations, we adopt one of the proposed methods to evaluate the linear gradient $\nabla \bar{q}_j$, and focus on the limiting function ϕ. The following subsection briefly describes a linear reconstruction procedure of $\nabla \bar{q}_j$.

2.2. Methods of linear reconstruction

The easiest method is to use the simple gradient operator by three cell-averaged values among T_j and its neighborhood [25,26].

$$\nabla \bar{q}_j = \begin{pmatrix} -\frac{n_1}{n_3} \\ -\frac{n_2}{n_3} \end{pmatrix}, \tag{6}$$

where n_1, n_2 and n_3 are the components of the vector $\mathbf{n}$ normal to the plane, which is given by

$$\mathbf{n} = (\mathbf{P}_i - \mathbf{P}_j) \times (\mathbf{P}_k - \mathbf{P}_i), \mathbf{P}_i = \begin{pmatrix} x_i \\ y_i \\ q_i \end{pmatrix}. \tag{7}$$

This method needs little computational cost, but it is not clear which triangle (or combination of triangles) is the optimal choice for gradient operation: $(\Delta ABC), (\Delta ABO), (\Delta BCO), (\Delta CAO)$ (see Fig. 1). Moreover, the operation may not be robust and accurate especially on stretched triangular element. As a consequence, two methods are mainly used [35].

The first choice is to use the Green–Gauss integral formula which transforms a gradient operation into a simple line integration as follows

$$\nabla \bar{q}_j \simeq \frac{1}{|T_j|} \int_{T_j} \nabla \bar{q}_j \, dV = \int_{\partial T_j} \bar{q} \mathbf{n} \, dS. \tag{8}$$

The last term is then calculated by a well-known numerical integral formula, such as trapezoidal method. In the cell-centered finite volume method, the nodal values are obtained by summing the values of neighboring cells with the weighting of inversely proportional distance from vertex to centroid [36]

$$\hat{q}_{v_i} = \frac{\sum_k \bar{q}_k / r_{v_i,k}}{\sum_k r_{v_i,k}^{-1}}, \tag{9}$$

where $\hat{q}_{v_i}$ is the nodal value at the vertex v_i, and $r_{v_i,k}$ is the distance from the vertex v_i to the neighboring cell T_k.

The second choice is the least-square reconstruction, which gives the gradient approximation by fitting the values of the cell and its neighborhood. For a simple triangular grid, the gradient is estimated by applying Eq. (4) to the neighborhood of the cell

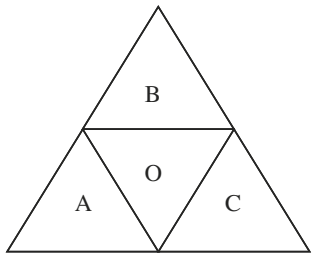

Fig. 1. Triangle cell T_0 and its neighborhood.

$$[\mathbf{L}_1\mathbf{L}_2]\nabla\bar{q}_j = \mathbf{f}, \tag{10}$$

where $\mathbf{L}_1 = [\Delta x_{OA}\Delta x_{OB}\Delta x_{OC}]^T$, $\mathbf{L}_2 = [\Delta y_{OA}\Delta y_{OB}\Delta y_{OC}]^T$ and $\mathbf{f} = [\bar{q}_A - \bar{q}_O\bar{q}_B - \bar{q}_O\bar{q}_C - \bar{q}_O]^T$. The least-square fitting of the above over-determined matrix gives an estimated gradient

$$\nabla\bar{q}_O = \frac{1}{l_{11}l_{22} - l_{12}^2}\begin{bmatrix} l_{22}(\mathbf{L}_1\cdot\mathbf{f}) - l_{12}(\mathbf{L}_2\cdot\mathbf{f}) \\ l_{11}(\mathbf{L}_2\cdot\mathbf{f}) - l_{12}(\mathbf{L}_1\cdot\mathbf{f}) \end{bmatrix}, \tag{11}$$

where $l_{ij} = \mathbf{L}_i^T\cdot\mathbf{L}_j$. For all its additional computational cost, the least-square technique is known to be more robust and less sensitive to grid irregularity [37]. Moreover, least-square reconstruction can be easily extended to quadratic- or higher-order reconstructions by including higher-order derivative terms [27,29].

3. Multi-dimensional limiting process on triangular meshes

3.1. Review of MLP on structured grids

The basic concept of MLP [33,34] is summarized in this subsection. For the purpose of brevity, it is explained in the two-dimensional setting but it is equally valid in three-dimensional case. We start by imagining a multi-dimensional situation where the direction of a local gradient is not aligned with local grid lines (see Fig. 2). This manifests the necessity to control the physical properties of cell-vertex points, which is not properly given by conventional TVD condition. To examine the missing information, we compare the MLP with TVD-MUSCL approach [38].

With symmetric MUSCL-type TVD limiters, the cell interface values can be obtained as follows

$$q^L_{i+1/2,j} = \bar{q}_{i,j} + \frac{1}{2}\varphi(r_L)\Delta\bar{q}_{i-1/2,j}, \quad q^R_{i+1/2,j} = \bar{q}_{i,j} - \frac{1}{2}\varphi(r_R)\Delta\bar{q}_{i+3/2,j}, \tag{12}$$

where $\Delta\bar{q}_{i-1/2,j} = \bar{q}_{i,j} - \bar{q}_{i-1,j}$, $r_L = \frac{\Delta\bar{q}_{i+1/2,j}}{\Delta\bar{q}_{i-1/2,j}}$ and $r_R = \frac{\Delta\bar{q}_{i+1/2,j}}{\Delta\bar{q}_{i+3/2,j}}$. The limiting function $\varphi(r)$ satisfies the symmetric condition of $\varphi(r) = r\varphi(1/r)$. One-dimensional limiting condition using the TVD constraint yields the following Sweby's TVD zone [10]

$$0 \leqslant \varphi(r) \leqslant \min(2r, 2). \tag{13}$$

Among several attempts to obtain monotonic solution in multi-dimensional space [22,23], MLP turned out to be one of the most successful ways to regulate spurious oscillations across multi-dimensional discontinuities. In Fig. 2, MLP applies the condition of Eq. (14) to each vertex point

$$\bar{q}^{\min}_{neighbor} \leqslant q_{vtx} \leqslant \bar{q}^{\max}_{neighbor}, \tag{14}$$

where q_{vtx} is the estimated-value at vertex, and $(\bar{q}^{\min}_{neighbor}, \bar{q}^{\max}_{neighbor})$ are the minimum and maximum values among the neighboring cell-averaged values sharing the vertex. A physical property at each vertex is then estimated by summing the monotonic variations along each coordinate direction, and the MLP condition of Eq. (14) is applied. Through some analysis using the TVD-MUSCL framework, the *variable* limiting region of Eq. (15) is obtained

$$0 \leqslant \varphi(r) \leqslant \min(\alpha r, \alpha). \tag{15}$$

α is the multi-dimensional restriction coefficient which determines the baseline variable limiting region. Detailed derivation of α (or α_L, α_R in Eq. (16)) for general two- and three-dimensional flow situations can be found in Ref. [34]. From Eqs. (13) and (15), one can see that the MLP limiting region is determined depending on local multi-dimensional flow physics, while TVD provides a *fixed* limiting region (see Fig. 3). Finally, local slopes (β_L, β_R in Eq. (16)) of MLP limiters can be determined in var-

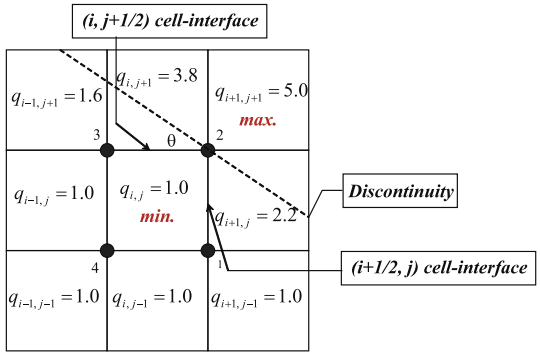

Fig. 2. A multi-dimensional flow situation where flow gradient is not aligned with local grid lines.

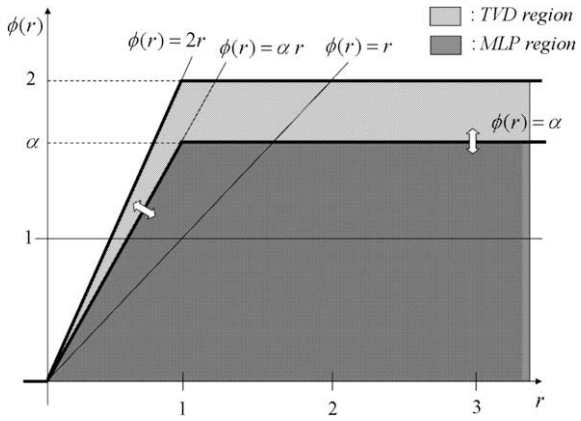

Fig. 3. Variable MLP limiting region.

ious ways. One may use slopes of conventional TVD limiters or slopes based on local higher-order polynomials. Choices of slopes can be found in Refs. [33,34]. Then, the cell interface flux by the MLP limiting is obtained as follows

$$q^L_{i+1/2,j} = \bar{q}_{i,j} + \frac{1}{2}\varphi(r_{L_{i,j}}, \alpha_L, \beta_L)\Delta\bar{q}_{i-1/2,j} = \bar{q}_{i,j} + \frac{1}{2}\max(0, \min(\alpha_L r_{L_{i,j}}, \alpha_L, \beta_L))\Delta\bar{q}_{i-1/2,j},$$
$$q^R_{i+1/2,j} = \bar{q}_{i,j} - \frac{1}{2}\varphi(r_{R_{i+1,j}}, \alpha_R, \beta_R)\Delta\bar{q}_{i+3/2,j} = \bar{q}_{i,j} - \frac{1}{2}\max(0, \min(\alpha_R r_{R_{i+1,j}}, \alpha_R, \beta_R))\Delta\bar{q}_{i+3/2,j}. \tag{16}$$

3.2. MLP condition on unstructured grids and the maximum principle

There are some additional difficulties to extend the MLP condition onto unstructured grids. Most notably, there is no explicit reference direction, and as a result, some key variables, such as α and β in Eq. (16), can not be derived step by step. Thus, we start from the MUSCL-type framework on unstructured meshes.

From the MLP formulation on structured grids [33,34], it was observed that the maximum and minimum values along the cell boundary should be examined to prevent spurious oscillations. In the MUSCL-type linear reconstruction, local extrema occur at vertex, and thus only the vertex value is limited by the MLP condition. By considering all of the neighboring cells sharing the vertex, the range of the multi-dimensional slope limiter can be obtained. Applying the MLP condition (Eq. (14)) to Eq. (4), the permissible range can be expressed as follows

$$\frac{\bar{q}^{\min}_{neighbor} - \bar{q}}{\nabla q \cdot \mathbf{r}_{vertex}} \leqslant \phi \leqslant \frac{\bar{q}^{\max}_{neighbor} - \bar{q}}{\nabla q \cdot \mathbf{r}_{vertex}}. \tag{17}$$

The effectiveness of the MLP condition is supported by the maximum principle, which is a complementary condition ensuring the monotonicity in multiple dimensions. This can be proved by taking a similar step shown in Refs. [39,35]. For the purpose of simplicity, we consider two-dimensional case but the result can be equally extended to three-dimensional tetrahedral meshes. Let us consider the following scalar hyperbolic conservation law in two-dimensional space

$$\frac{\partial q}{\partial t} + \frac{\partial f(q)}{\partial x} + \frac{\partial g(q)}{\partial y} = 0. \tag{18}$$

Theorem. *For a fully discrete finite volume scheme of Eq. (18) with a monotone Lipschitz continuous flux function, if the linear reconstruction satisfies the MLP condition under a proper CFL restriction, then the scheme satisfies the maximum principle, i.e.,*

$$\bar{q}^{\min,n}_{j,neighbor} \leqslant \bar{q}^{n+1}_j \leqslant \bar{q}^{\max,n}_{j,neighbor}. \tag{19}$$

$\bar{q}^{min}_{j,neighbor}$ and $\bar{q}^{max}_{j,neighbor}$ are the minimum and maximum cell-averaged values among the neighborhood of the cell T_j which shares at least one common vertex with the cell T_j (see the shaded region in Fig. 4).

Proof. Consider the semi-discrete form of Eq. (18) on the cell T_j.

$$|T_j|\frac{\partial \bar{q}_j}{\partial t} + \sum_{e_{jk}\in T_j} h(\bar{q}_{jk}, \bar{q}_{kj})|e_{jk}| = 0, \tag{20}$$

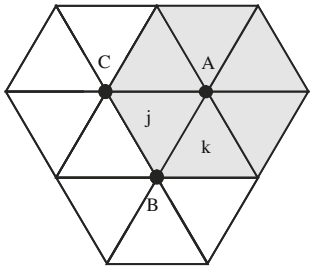

Fig. 4. Neighborhood of the cell T_j (shaded region: group of cells sharing the vertex A).

where $\bar{q}_{jk}$ is the cell interface value in the direction from the cell T_j to the cell T_k, and $h(\bar{q}_{jk}, \bar{q}_{kj})$ is a numerical flux function. $\bar{q}_{jk}$ is assumed to be located at the center of a cell interface since the numerical flux is obtained by the midpoint rule.

Let $\hat{q}_{v_i j}$ denote the estimated-value at the vertex v_i of the cell T_j after the limiting process. From the MLP condition, it should satisfy the following inequality.

$$\hat{q}_{v_i}^{\min} \leqslant \hat{q}_{v_i j} \leqslant \hat{q}_{v_i}^{\max}, \tag{21}$$

where $\hat{q}_{v_i}^{\min}$ and $\hat{q}_{v_i}^{\max}$ are the minimum and maximum cell-averaged values among the cells sharing the vertex v_i. Then, $\bar{q}_{j,neighbor}^{\min}$ and $\bar{q}_{j,neighbor}^{\max}$ can be written as

$$\bar{q}_{j,neighbor}^{\min} = \min_{v_i \in T_j}(\hat{q}_{v_i}^{\min}), \quad \bar{q}_{j,neighbor}^{\max} = \max_{v_i \in T_j}(\hat{q}_{v_i}^{\max}). \tag{22}$$

From the linear reconstruction, the cell interface values are expressed as a linear combination of the vertex values

$$\bar{q}_{jk} = \xi \hat{q}_{v_1 j} + (1-\xi)\hat{q}_{v_2 j}, \quad 0 \leqslant \xi \leqslant 1, \tag{23}$$

$$\bar{q}_{kj} = \zeta \hat{q}_{v_1 k} + (1-\zeta)\hat{q}_{v_2 k}, \quad 0 \leqslant \zeta \leqslant 1. \tag{24}$$

With Eqs. (21) and (22), the interface values are bounded as

$$\bar{q}_{j,neighbor}^{\min} \leqslant \bar{q}_{jk}, \quad \bar{q}_{kj} \leqslant \bar{q}_{j,neighbor}^{\max}. \tag{25}$$

By applying Eq. (25) and the monotonicity of the numerical flux function to Eq. (20), the following relation can be obtained.

$$\begin{aligned}
\frac{\partial \bar{q}_j}{\partial t} &= -\frac{1}{|T_j|}\sum_{e_{jk}\in T_j} h(\bar{q}_{jk}, \bar{q}_{kj})|e_{jk}| \leqslant -\frac{1}{|T_j|}\sum_{e_{jk}\in T_j} h\left(\min_k(\bar{q}_{jk}), \bar{q}_{j,neighbor}^{\max}\right)|e_{jk}| \\
&= -\frac{1}{|T_j|}\sum_{e_{jk}\in T_j}\left\{h\left(\min_k(\bar{q}_{jk}), \bar{q}_{j,neighbor}^{\max}\right) - h\left(\min_k(\bar{q}_{jk}), \min_k(\bar{q}_{jk})\right)\right\}|e_{jk}| \\
&= -\frac{1}{|T_j|}\sum_{e_{jk}\in T_j}\frac{\partial h}{\partial q}\left(\min_k(\bar{q}_{jk}), \xi\right)\left(\bar{q}_{j,neighbor}^{\max} - \min_k(\bar{q}_{jk})\right)|e_{jk}| \\
&\leqslant \frac{L_j}{|T_j|}\sup_{\xi\in\left[\min_k(\bar{q}_{jk}), \bar{q}_{j,neighbor}^{\max}\right]}\left|\frac{\partial h}{\partial q}(\min_k(\bar{q}_{jk}), \xi)\right|(\bar{q}_{j,neighbor}^{\max} - \min_k(\bar{q}_{jk})),
\end{aligned} \tag{26}$$

where L_j is the perimeter of T_j.

In a similar manner, we can obtain another inequality.

$$\frac{\partial \bar{q}_j}{\partial t} \geqslant \frac{L_j}{|T_j|}\sup_{\xi\in\left[\bar{q}_{j,neighbor}^{\min}, \max_k(\bar{q}_{jk})\right]}\left|\frac{\partial h}{\partial q}(\max_k(\bar{q}_{jk}), \xi)\right|\left(\bar{q}_{j,neighbor}^{\min} - \max_k(\bar{q}_{jk})\right). \tag{27}$$

If we apply the simple Euler explicit time integration to Eq. (20) under the following CFL condition,

$$\Delta t \frac{L_j}{|T_j|}\left(\sup_{q_1, q_2 \in \left[\bar{q}_{j,neighbor}^{\min}, \bar{q}_{j,neighbor}^{\max}\right]}\left|\frac{\partial h}{\partial q_2}(q_1, q_2)\right|\right) \leqslant \frac{1}{3}, \tag{28}$$

the two inequalities, Eqs. (26) and (27), can be combined as

$$\frac{1}{3}\left(\bar{q}_{j,neighbor}^{\min,n} - \max_k(\bar{q}_{jk}^n)\right) \leqslant \bar{q}_j^{n+1} - \bar{q}_j^n \leqslant \frac{1}{3}\left(\bar{q}_{j,neighbor}^{\max,n} - \min_k(\bar{q}_{jk}^n)\right). \tag{29}$$

Since $\bar{q}_{jk}^n$ is located at the edge midpoint, we have

$$\frac{1}{3}\sum_{e_{jk}\in T_j}\bar{q}_{jk}^n = \frac{1}{3}\sum_{e_{jk}\in T_j}\left(\bar{q}_j^n + \nabla\bar{q}_j^n\cdot\mathbf{r}_{jk}\right) = \bar{q}_j^n. \tag{30}$$

Thus, the right hand side of Eq. (29) can be further simplified into the following expression

$$\begin{aligned}\bar{q}_{j,neighbor}^{\max,n} - \min_k(\bar{q}_{jk}^n) &= \bar{q}_{j,neighbor}^{\max,n} - \frac{1}{3}\sum_{e_{jk}\in T_j}\left\{\min_k\left(\bar{q}_{jk}^n\right) + \bar{q}_{jk}^n - \bar{q}_{jk}^n\right\} = \bar{q}_{j,neighbor}^{\max,n} - \bar{q}_j^n + \frac{1}{3}\sum_{e_{jk}\in T_j}\left\{\bar{q}_{jk}^n - \min_k(\bar{q}_{jk}^n)\right\}\\ &\leqslant \bar{q}_{j,neighbor}^{\max,n} - \bar{q}_j^n + \frac{1}{3}\left\{2\bar{q}_{j,neighbor}^{\max,n} + \min_k(\bar{q}_{jk}^n) - 3\min_k(\bar{q}_{jk}^n)\right\} = \bar{q}_{j,neighbor}^{\max,n} - \bar{q}_j^n + \frac{2}{3}\left(\bar{q}_{j,neighbor}^{\max,n} - \min_k(\bar{q}_{jk}^n)\right).\end{aligned} \tag{31}$$

Thus, we have

$$\frac{1}{3}\left(\bar{q}_{j,neighbor}^{\max,n} - \min_k(\bar{q}_{jk}^n)\right) \leqslant \bar{q}_{j,neighbor}^{\max,n} - \bar{q}_j^n. \tag{32}$$

Similarly, the left hand side of Eq. (29) can be expressed as

$$\frac{1}{3}\left(\bar{q}_{j,neighbor}^{\min,n} - \max_k(\bar{q}_{jk}^n)\right) \geqslant \bar{q}_{j,neighbor}^{\min,n} - \bar{q}_j^n. \tag{33}$$

Inserting Eqs. (32) and (33) into Eq. (29), the $(n+1)^{th}$ cell-averaged value is bounded by the minimum and maximum cell-averaged values among the neighborhood of the cell T_j at n step.

$$\bar{q}_{j,neighbor}^{\min,n} \leqslant \bar{q}_j^{n+1} \leqslant \bar{q}_{j,neighbor}^{\max,n}. \tag{34}$$

Thus, the MLP limiting satisfies the maximum principle. □

The above result relies on two assumptions: one is that grid system consists of triangular elements only, and the other is that a numerical flux is calculated by the midpoint rule. However, these restrictions can be relieved by employing the Barth's geometric shape parameter [35]

$$\Gamma^{geom} = \sup_{0\leqslant\theta\leqslant 2\pi}\alpha^{-1}(\theta). \tag{35}$$

α indicates the smallest fractional perpendicular distance from the center to one of the two minimally separated parallel hyperplanes with the orientation of θ. With Γ^{geom}, the CFL condition (Eq. (28)) can be generalized as follows

$$\Delta t\frac{L_j}{|T_j|}\left(\sup_{q_1,q_2\in\left[\bar{q}_{j,neighbor}^{\min},\bar{q}_{j,neighbor}^{\max}\right]}\left|\frac{\partial h}{\partial q_2}(q_1,q_2)\right|\right) \leqslant \frac{1}{\Gamma^{geom}}. \tag{36}$$

For triangular mesh, the geometric shape parameter becomes 3, which is exactly the same as the CFL condition. Thus, Eq. (29) becomes

$$\frac{1}{\Gamma^{geom}}\left(\bar{q}_{j,neighbor}^{\min,n} - \max_k(\bar{q}_{jk}^n)\right) \leqslant q_j^{n+1} - q_j^n \leqslant \frac{1}{\Gamma^{geom}}\left(\bar{q}_{j,neighbor}^{\max,n} - \min_k(\bar{q}_{jk}^n)\right). \tag{37}$$

From the definition of Γ^{geom} and the linear reconstruction of $\bar{q}_j$, the right hand side of Eq. (37) is given by

$$\begin{aligned}\bar{q}_{j,neighbor}^{\max,n} - \min_k(\bar{q}_{jk}^n) &= \left(\bar{q}_{j,neighbor}^{\max,n} - \bar{q}_j^n\right) + \left(\bar{q}_j^n - \min_k(\bar{q}_{jk}^n)\right) \leqslant \left(\bar{q}_{j,neighbor}^{\max,n} - \bar{q}_j^n\right) + \gamma^{geom}\left(\max_k(\bar{q}_{jk}^n) - \min_k(\bar{q}_{jk}^n)\right)\\ &\leqslant \left(\bar{q}_{j,neighbor}^{\max,n} - \bar{q}_j^n\right) + \gamma^{geom}\left(\bar{q}_{j,neihbor}^{\max,n} - \min_k(\bar{q}_{jk}^n)\right),\end{aligned} \tag{38}$$

where $\gamma^{geom} = (\Gamma^{geom}-1)/\Gamma^{geom}$. It is noted that Eq. (38) does not require $\bar{q}_{jk}^n$ to be located at the edge midpoint. And, we have

$$\bar{q}_{j,neighbor}^{\max,n} - \min_k(\bar{q}_{jk}^n) \leqslant \Gamma^{geom}\left(\bar{q}_{j,neighbor}^{\max,n} - \bar{q}_j^n\right). \tag{39}$$

Similarly, the left hand side of Eq. (37) can be rewritten as

$$\bar{q}_{j,neighbor}^{\min,n} - \max_k(\bar{q}_{jk}^n) \geqslant \Gamma^{geom}\left(\bar{q}_{j,neighbor}^{\min,n} - \bar{q}_j^n\right). \tag{40}$$

Inserting Eqs. (39) and (40) into Eq. (37) leads to the maximum principle of Eq. (34) in general case. All of the processes from Eqs. (36)–(40) can be equally extended into three-dimensional tetrahedral meshes with $\Gamma^{geom} = 4$. Thus, the MLP limiting satisfies the maximum principle under general condition not only on triangular meshes but also on three-dimensional tetrahedral meshes. It also shows that the process from Eqs. (30)–(33) can be obtained by using geometric characteristics.

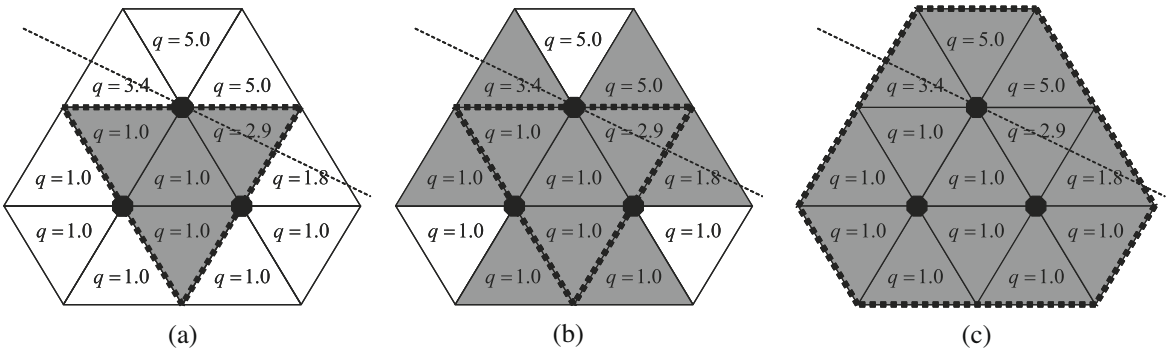

Fig. 5. Comparison of stencils involved in limiting and the maximum principle. Shaded region is the stencil for the maximum principle, and dotted line is for limiting. (a) LCD, MLG limiter, (b) Barth's limiter and (c) MLP limiting.

Other limiters for unstructured grids, such as Barth limiter,[1] LCD and MLG limiters [25,26], also satisfy the maximum principle. The essential difference is the stencil involved in limiting and the maximum principle (see Fig. 5). Since the permissible limiting range of these limiters essentially comes from the Spekreijse's monotonic condition [23], only the neighboring cells which share one of the edges of the updated cell are considered. Thus, they may have drawbacks in capturing multi-dimensional flow physics. On the other hand, the MLP condition fully exploits all of the cell-averaged values sharing vertices as well as edges. More importantly, the stencils involved in limiting and the maximum principle are equivalent. As a result, the MLP limiting is less sensitive to local mesh distribution and faithfully represents multi-dimensional flow physics. Detailed numerical comparisons are provided in Section 4.

3.3. General formulation of MLP on unstructured grids

By implementing the MLP condition into the MUSCL-type framework, the general formulation of the MLP slope limiter can be expressed as follows

$$\phi_{\mathrm{MLP}} = \min_{\forall v_i \in T_j} \begin{cases} \Phi(r^{\max}_{v_i j}) & \text{if } \nabla \bar{q}_j \cdot \mathbf{r}_{v_i j} > 0 \\ \Phi(r^{\min}_{v_i j}) & \text{if } \nabla \bar{q}_j \cdot \mathbf{r}_{v_i j} < 0 \\ 1 & \text{otherwise} \end{cases}, \tag{41}$$

where $r^{\min \text{ or } \max}_{v_i j}$($r^{\min}_{v_i j}$ or $r^{\max}_{v_i j}$) is the ratio of the allowable variation to the estimated variation at the vertex v_i. In Eq. (41), $r^{\min \text{ or } \max}_{v_i j}$ and $\Phi(r^{\min \text{ or } \max}_{v_i j})$ have to be specified. This bears some analogy to the determination of α and β in Eq. (16) on structured meshes. In MLP, the ratio $r^{\min \text{ or } \max}_j$ is defined by

$$r^{\min}_{v_i j} = \frac{\hat{q}^{\min}_{v_i} - \bar{q}_j}{\nabla \bar{q}_j \cdot \mathbf{r}_{v_i j}}, \quad r^{\max}_{v_i j} = \frac{\hat{q}^{\max}_{v_i} - \bar{q}_j}{\nabla \bar{q}_j \cdot \mathbf{r}_{v_i j}}. \tag{42}$$

Eq. (42) is similar to other limiters, but the basic differences are, as shown in Fig. 5, the location where the limiter is working and the stencil to determine $\hat{q}^{\min}_{v_i}$ and $\hat{q}^{\max}_{v_i}$. From the definition of $r^{\min \text{ or } \max}_{v_i j}$, one can readily see that the allowable limiting region satisfying the maximum principle should be given by $0 \leqslant \Phi(r^{\min \text{ or } \max}_{v_i j}) \leqslant \min(1, r^{\min \text{ or } \max}_{v_i j})$ for each vertex v_i. As a local slope, two candidates are considered. The first one is $\min(1, r^{\min \text{ or } \max}_{v_i j})$, which is the most upper slope in the allowable limiting region. This limiter is denoted as MLP-u1

$$\Phi(r^{\min \text{ or } \max}_{v_i j})_{\text{MLP-u1}} = \min(1, r^{\min \text{ or } \max}_{v_i j}). \tag{43}$$

MLP-u1 is not differentiable, which may have problems in steady state computations. By employing the Venkatakrishnan's modification of the Barth's limiter [24], MLP-u2 (or MLP-Venkatakrishnan) limiter is proposed for steady state computations

$$\Phi\left(\frac{\Delta_+}{\Delta_-}\right)_{\text{MLP-u2}} = \frac{1}{\Delta_-}\left[\frac{(\Delta_+^2 + \epsilon^2)\Delta_- + 2\Delta_-^2\Delta_+}{\Delta_+^2 + 2\Delta_-^2 + \Delta_-\Delta_+ + \epsilon^2}\right], \tag{44}$$

where $\Delta_+ = \hat{q}^{\min \text{ or } \max}_{v_i} - \bar{q}_j, \Delta_- = \nabla \bar{q}_j \cdot \mathbf{r}_{v_i j}. \epsilon = (K\Delta x)^r$ with $r = 1.5$. The role of ϵ is to distinguish a nearly constant region from a fluctuating one. Like TVB or ELED limiters, it also plays a role of preventing the clipping phenomenon [22,24].

From the observation that the stencils involved in limiting and the maximum principle are the same, and the MLP stencil is more compact and multi-dimensional, one may expect that the MLP slope is greater than the slope of conventional limiter, such as Barth limiter and Venkatakrisnan limiter. Regarding this, the following result can be presented.

[1] Except for the maximum principle, similar limiting strategy was also proposed along an edge within MUSCL-FEM framework [18].

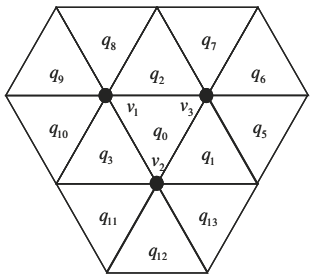

Fig. 6. MLP stencil around the cell T_0.

Lemma 1. *Let a linear reconstruction of* $q_0(x,y) = \bar{q}_0 + \phi\nabla\bar{q}_0 \cdot \mathbf{r}$ *on the stencil in Fig. 6 satisfy the following two conditions.*

- $C1$: The vertex value of T_0 opposite to the maximum neighboring cell-centered value of T_0 is less than $\bar{q}_0$.
- $C2$: The vertex value of T_0 opposite to the minimum neighboring cell-centered value of T_0 is greater than $\bar{q}_0$.

Then, the allowable variation$(\phi\nabla\bar{q}_0 \cdot \mathbf{r})$ *obtained by the MLP limiting from the cell centroid to each vertex is greater than that of conventional (Barth or Venkatakrisnan) limiting. Thus,* $\phi_{\text{MLP-u1}}$ *(or* $\phi_{\text{MLP-u2}}$*) is less diffusive than* ϕ_{Barth} *(or* $\phi_{Venkatakrishnan}$*).*

Proof. Let us consider the stencil, as shown in Fig. 6, around the cell T_0 whose vertex is (v_1, v_2, v_3), respectively. $q_0(x,y)$ is the least-square reconstruction of $\bar{q}_0$ using $\bar{q}_0, \bar{q}_1, \bar{q}_2, \bar{q}_3$. If $\bar{q}_0$ is the local extremum, the allowable variation becomes zero to yield the first order accuracy. If the local extremum is one of $(\bar{q}_1, \bar{q}_2, \bar{q}_3)$, we may assume, without loss of generality, that $\bar{q}_1 = \max(\bar{q}_0, \bar{q}_1, \bar{q}_2, \bar{q}_3)$ and $\bar{q}_2 = \min(\bar{q}_0, \bar{q}_1, \bar{q}_2, \bar{q}_3)$. From the conditions $C1$ and $C2$, we have

$$\nabla\bar{q}_0 \cdot \mathbf{r}_{v_1,0} < 0 \text{ and } \nabla\bar{q}_0 \cdot \mathbf{r}_{v_2,0} > 0. \tag{45}$$

The maximum allowable variation, which is simply the numerator of $r_{v_i j}^{\min \text{ or } \max}$ in Eq. (42), determines the maximum allowable slope. The original form of Barth limiter [20], which uses vertex for limiting procedure, is compared with the MLP limiter. Then, the maximum allowable variation can be written as follows

$$\Delta_{Barth} = \begin{cases} \max(\bar{q}_0, \bar{q}_1, \bar{q}_2, \bar{q}_3) - \bar{q}_0 & \text{if } \nabla\bar{q}_0 \cdot \mathbf{r}_{v_i,0} > 0 \\ \min(\bar{q}_0, \bar{q}_1, \bar{q}_2, \bar{q}_3) - \bar{q}_0 & \text{if } \nabla\bar{q}_0 \cdot \mathbf{r}_{v_i,0} < 0 \\ 0 & \text{otherwise} \end{cases}. \tag{46}$$

$$\Delta_{\text{MLP}} = \begin{cases} \hat{q}_{v_i}^{\max} - \bar{q}_0 & \text{if } \nabla\bar{q}_0 \cdot \mathbf{r}_{v_i,0} > 0 \\ \hat{q}_{v_i}^{\min} - \bar{q}_0 & \text{if } \nabla\bar{q}_0 \cdot \mathbf{r}_{v_i,0} < 0 \\ 0 & \text{otherwise} \end{cases}. \tag{47}$$

For the vertex v_1,

$$\min(\bar{q}_0, \bar{q}_1, \bar{q}_2, \bar{q}_3) = \bar{q}_2 \geqslant \min(\bar{q}_0, \bar{q}_2, \bar{q}_3, \bar{q}_8, \bar{q}_9, \bar{q}_{10}) = \hat{q}_{v_1}^{\min}. \tag{48}$$

For the vertex v_2,

$$\max(\bar{q}_0, \bar{q}_1, \bar{q}_2, \bar{q}_3) = \bar{q}_1 \leqslant \max(\bar{q}_0, \bar{q}_1, \bar{q}_3, \bar{q}_{11}, \bar{q}_{12}, \bar{q}_{13}) = \hat{q}_{v_2}^{\max}. \tag{49}$$

And, for the vertex v_3,

$$\min(\bar{q}_0, \bar{q}_1, \bar{q}_2, \bar{q}_3) = \bar{q}_2 \geqslant \min(\bar{q}_0, \bar{q}_1, \bar{q}_2, \bar{q}_5, \bar{q}_6, \bar{q}_7) = \hat{q}_{v_3}^{\min}, \tag{50}$$

$$\max(\bar{q}_0, \bar{q}_1, \bar{q}_2, \bar{q}_3) = \bar{q}_1 \leqslant \max(\bar{q}_0, \bar{q}_1, \bar{q}_2, \bar{q}_5, \bar{q}_6, \bar{q}_7) = \hat{q}_{v_3}^{\max}. \tag{51}$$

From Eqs. (48)–(51), $|\Delta_{\text{MLP}}|$ is greater than $|\Delta_{Barth}|$ at all vertices of the cell T_0, and Φ in Eqs. (43) and (44) is the same for MLP and conventional limiting. Thus, $\phi_{\text{MLP-u1}}$(or $\phi_{\text{MLP-u2}}$) $\geqslant \phi_{Barth}$(or $\phi_{Venkatakrishnan}$). □

The two conditions $(C1, C2)$ are not restrictive. They readily holds for equilateral triangles, and are generally satisfied unless meshes are far from equilateral and highly distorted. It is noted that the above result can be similarly extended into three-dimensional tetrahedral meshes.

In summary, the implementation step of the MLP limiting strategy can be described as follows.

Step 1: For each cell T_j in the computational domain, obtain gradient by the methods of linear reconstruction described in Section 2.2.

Step 2: For each vertex v_i of the cell T_j, search the minimum $(\hat{q}_{v_i}^{\min})$ and the maximum $(\hat{q}_{v_i}^{\max})$ by checking all the neighboring cells which share the vertex v_i.

Step 3: For each vertex v_i of the cell T_j, obtain $r_{v_i,j}^{\min \text{ or } \max}$ in Eq. (42) and determine the allowable local slope using Eq. (43) or Eq. (44). Then, ϕ_{MLP} takes the minimum value among the allowable slopes using Eq. (41).

Step 4: For each edge e_{jk} of the cell T_j, obtain $\bar{q}_{jk} = \bar{q}_j + \phi_{\text{MLP}} \nabla \bar{q}_j \cdot \mathbf{r}_{jk}$ and evaluate the numerical flux $h(\bar{q}_{jk}, \bar{q}_{kj})$ at the edge midpoint.

4. Numerical results

Extensive numerical experiments have been carried out to demonstrate the performance of the newly proposed MLP-u limiters on unstructured grids. Test cases include linear wave problem, shock tube problems, isentropic vortex problem and other well-known numerical test cases. Accuracy and convergence characteristics of MLP-u limiters are compared with conventional limiters such as Barth's limiter [20] or Venkatakrishnan's limiter [24]. Unless mentioned otherwise, conservative variables are used for interpolation. Lax–Friedrichs scheme, Roe-type schemes [40,41] and AUSM-type scheme [42] are adopted as numerical fluxes. As a time integration method, third-order TVD Runge–Kutta method [43] is used for unsteady calculation, and Gauss–Seidel method [44] is used for steady calculation.

4.1. Linear wave problem

A scalar linear wave problem governed by the following equation is considered

$$q_t + \mathbf{a} \cdot \nabla q = 0, \tag{52}$$

with constant wave velocity **a**. The numerical flux is calculated by an upwind scheme and the third-order accurate TVD Runge–Kutta time integration is used.

Computation domain is $[0,1] \times [0,1]$ and periodic boundary condition is applied. In order to examine grid dependency, three types of meshes, whose triangular elements are created by dividing rectangular elements along the diagonal direction, are tested (see Fig. 7). To avoid mesh alignment, the advection velocity is chosen as $\mathbf{a} = (1,2)$ [26]. Coefficient of Venkatakrishnan's limiter is 0.1. Two examples with smooth and discontinuous initial data are considered.

4.1.1. Double sine wave

The initial profile of the wave is given as follows

$$q_0 = sin(2\pi x) sin(2\pi y). \tag{53}$$

Figs. 8–10 show computed solutions with $20 \times 20 \times 2$ grids at $t = 1$, when the periodic wave returns to the initial location. Depending on mesh distribution, computed contours are somewhat distorted along the diagonal direction. Compared with Barth's limiter and Venkatakrishnan's limiter, the results of MLP-u limiters are less sensitive to the mesh distribution. Tables 1–3 show quantitative comparisons of solution errors at $t = 1$. MLP-u limiters yield a significant improvement over conventional limiters, which confirms the robustness and accuracy of the MLP formulation. Venkatakrishnan's modification is slightly more diffusive than the baseline limiter, but it does not seem to seriously hamper the solution accuracy.

4.1.2. Square wave

To examine oscillatory behavior across a discontinuity, square wave advection is considered with the following initial data

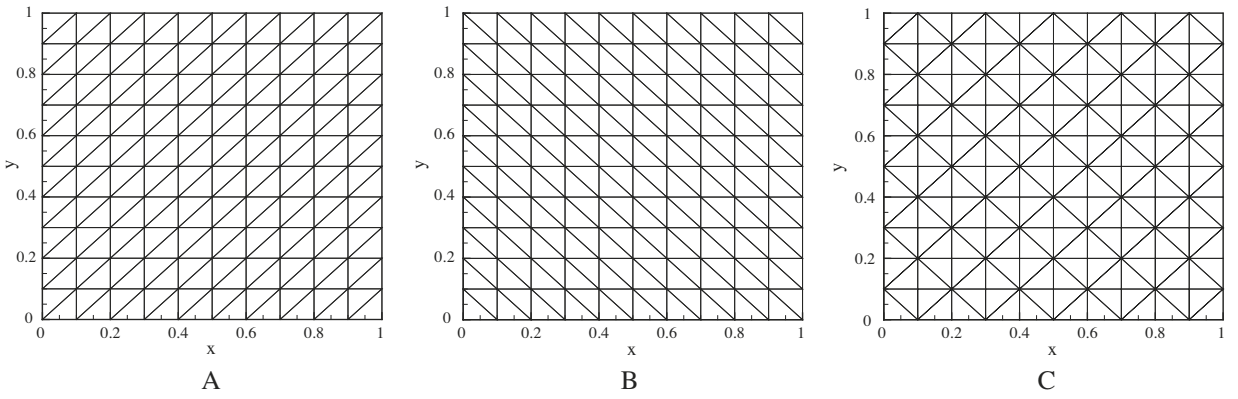

Fig. 7. Grid types by dividing rectangular element.

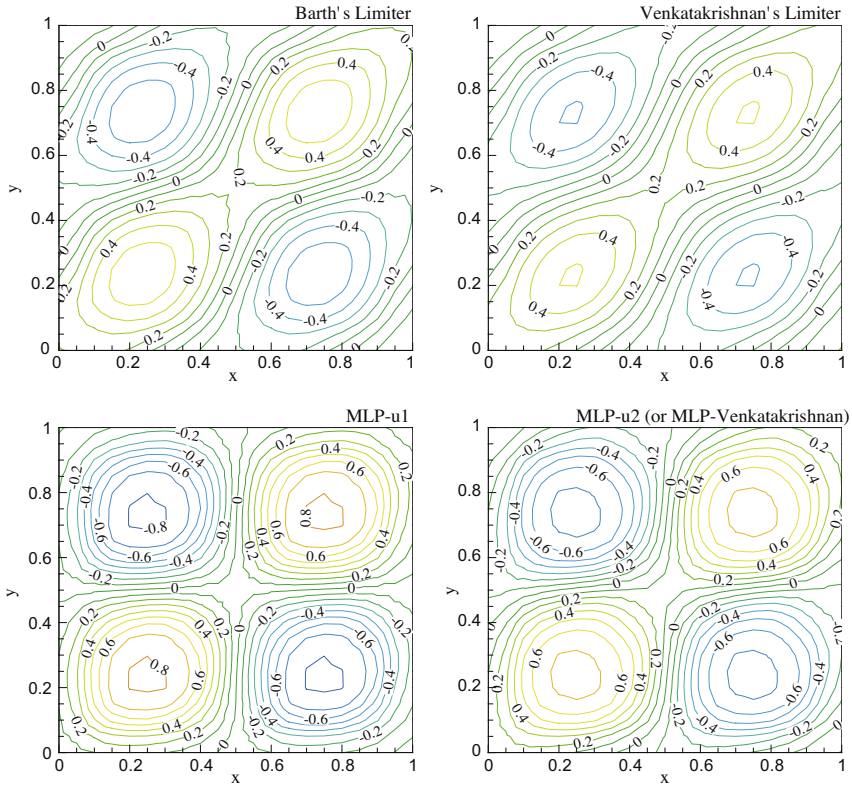

Fig. 8. Comparison of contour on grid type A (double sine wave).

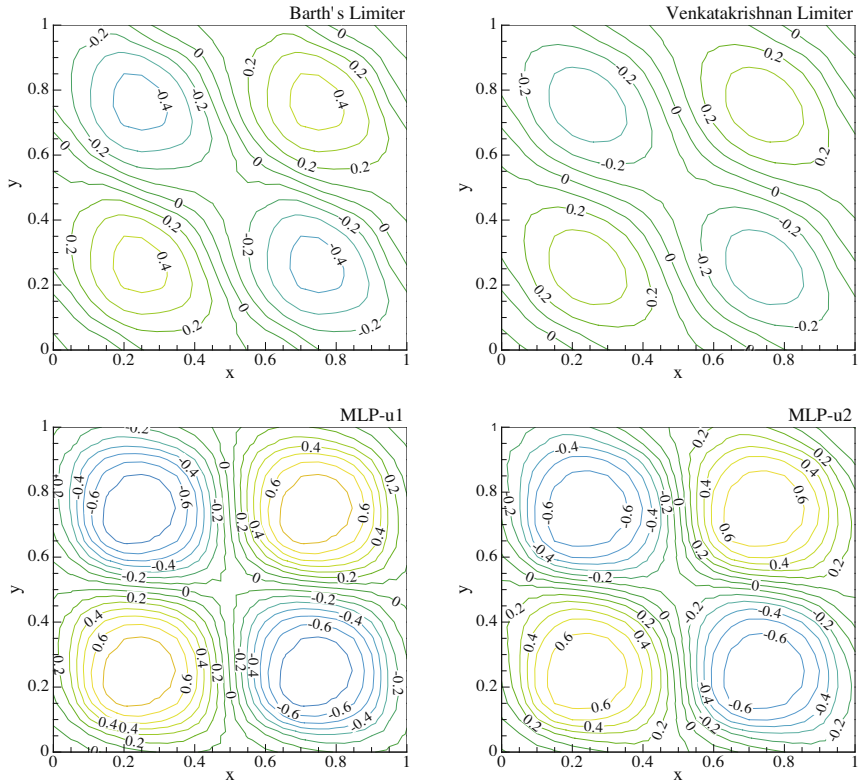

Fig. 9. Comparison of contour on grid type B (double sine wave).

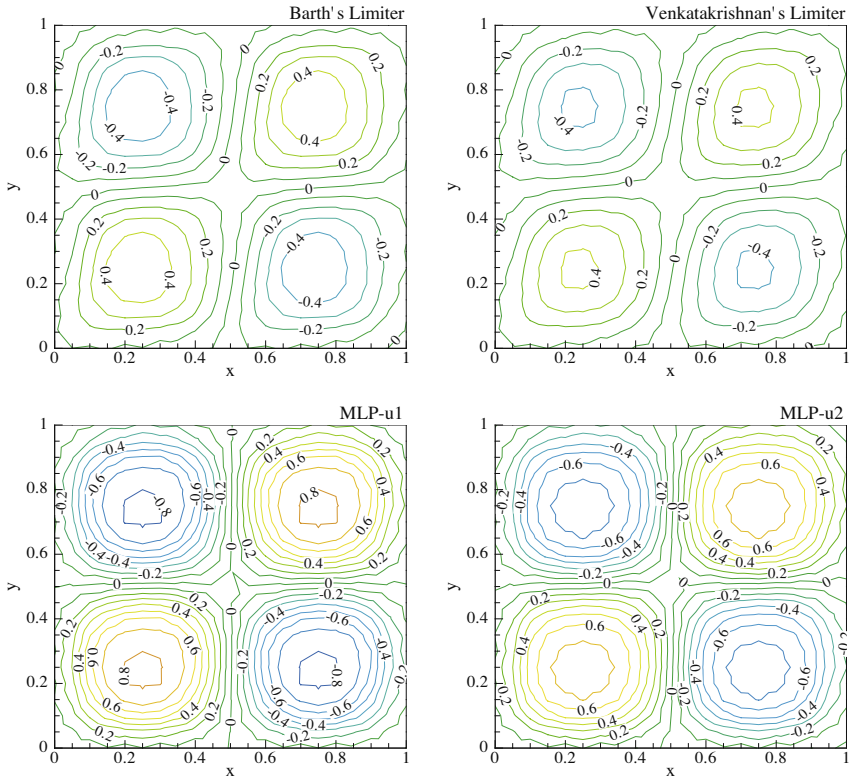

Fig. 10. Comparison of contour on grid type C (double sine wave).

Table 1
Grid refinement test for the advection of double sine wave on grid type A.

Scheme	Grid	L_∞	Order	L_1	Order	Peak
Barth's limiter	20 × 20 × 2	4.0857E−01	–	1.8795E−01	–	0.5896
	40 × 40 × 2	2.3275E−01	0.81	1.1570E−01	0.70	0.7683
	80 × 80 × 2	1.3716E−01	0.76	6.6048E−02	0.81	0.8762
	160 × 160 × 2	7.7957E−02	0.81	3.6023E−02	0.87	0.9365
Venkatakrishnan's limiter	20 × 20 × 2	4.7878E−01	–	2.2160E−01	–	0.5190
	40 × 40 × 2	2.8812E−01	0.73	1.4261E−01	0.64	0.7127
	80 × 80 × 2	1.6062E−01	0.84	8.2375E−02	0.79	0.8447
	160 × 160 × 2	8.9043E−02	0.85	4.4656E−02	0.88	0.9194
MLP-u1	20 × 20 × 2	1.7544E−01	–	3.3721E−02	–	0.8153
	40 × 40 × 2	6.6036E−02	1.41	6.5248E−03	2.37	0.9317
	80 × 80 × 2	2.3412E−02	1.50	1.2439E−03	2.39	0.9760
	160 × 160 × 2	8.0831E−03	1.53	2.5402E−04	2.29	0.9918
MLP-u2	20 × 20 × 2	2.5789E−01	–	7.0173E−02	–	0.7325
	40 × 40 × 2	1.0727E−01	1.27	1.6780E−02	2.06	0.8906
	80 × 80 × 2	4.3619E−02	1.30	4.1919E−03	2.00	0.9559
	160 × 160 × 2	1.7198E−02	1.34	9.7094E−04	2.11	0.9827
Unlimited (least-square)	20 × 20 × 2	3.2729E−02	–	1.7253E−02	–	0.9663
	40 × 40 × 2	6.5138E−03	2.33	3.4741E−03	2.31	0.9946
	80 × 80 × 2	1.4691E−03	2.15	8.0518E−04	2.11	0.9990
	160 × 160 × 2	3.5323E−04	2.06	1.9720E−04	2.03	0.9998

$$q_0 = \begin{cases} 1 & \text{if } -0.5 \leqslant x, y \leqslant 0, \\ 0 & \text{otherwise.} \end{cases} \tag{54}$$

Fig. 11 shows the computed advection of square wave at $t = 1$ with $80 \times 80 \times 2$ of type A grid. Both limiters give monotone solutions near the discontinuous profile but MLP-u limiter captures the discontinuity much more sharply. In Table 4, the maximum and minimum values are examined with three types of grids. It is observed that MLP-u limiters are less dissipative and accurately resolve the discontinuity without spurious oscillations.

Table 2
Grid refinement test for the advection of double sine wave on grid type B.

Scheme	Grid	L_∞	Order	L_1	Order	Peak
Barth's limiter	$20 \times 20 \times 2$	5.4313E−01	–	2.2965E−01	–	0.4551
	$40 \times 40 \times 2$	3.3255E−01	0.71	1.4527E−01	0.66	0.6710
	$80 \times 80 \times 2$	1.8415E−01	0.85	8.4258E−02	0.79	0.8197
	$160 \times 160 \times 2$	9.9818E−02	0.88	4.6634E−02	0.85	0.9070
Venkatakrishnan's limiter	$20 \times 20 \times 2$	6.1746E−01	–	2.6079E−01	–	0.3823
	$40 \times 40 \times 2$	3.8565E−01	0.68	1.7028E−01	0.61	0.6176
	$80 \times 80 \times 2$	2.1392E−01	0.85	9.9423E−02	0.78	0.7888
	$160 \times 160 \times 2$	1.1424E−01	0.90	5.4487E−02	0.87	0.8892
MLP-u1	$20 \times 20 \times 2$	2.2571E−01	–	5.1843E−02	–	0.7662
	$40 \times 40 \times 2$	8.3663E−02	1.43	1.0606E−02	2.29	0.9141
	$80 \times 80 \times 2$	2.9851E−02	1.49	2.2415E−03	2.24	0.9696
	$160 \times 160 \times 2$	1.0438E−02	1.52	4.8707E−04	2.20	0.9894
MLP-u2	$20 \times 20 \times 2$	3.0541E−01	–	8.5665E−01	–	0.6884
	$40 \times 40 \times 2$	1.2320E−01	1.31	2.4063E−02	1.83	0.8760
	$80 \times 80 \times 2$	4.9267E−02	1.32	7.3554E−03	1.71	0.9509
	$160 \times 160 \times 2$	1.9195E−02	1.36	1.9294E−03	1.93	0.9810
Unlimited (least-square)	$20 \times 20 \times 2$	8.3646E−02	–	4.2743E−02	–	0.9308
	$40 \times 40 \times 2$	1.6161E−03	2.37	7.8493E−03	2.45	0.9901
	$80 \times 80 \times 2$	3.5471E−03	2.19	1.7027E−03	2.20	0.9985
	$160 \times 160 \times 2$	8.4319E−04	2.07	4.0747E−03	2.06	0.9998

Table 3
Grid refinement test for the advection of double sine wave on grid type C.

Scheme	Grid	L_∞	Order	L_1	Order	Peak
Barth's limiter	$20 \times 20 \times 2$	5.1426E−01	–	1.9722E−01	–	0.4926
	$40 \times 40 \times 2$	3.2117E−01	0.68	1.1558E−01	0.77	0.6870
	$80 \times 80 \times 2$	1.8617E−01	0.79	6.5150E−02	0.83	0.8218
	$160 \times 160 \times 2$	1.0461E−01	0.83	3.5483E−02	0.88	0.9050
Venkatakrishnan's limiter	$20 \times 20 \times 2$	5.6554E−01	–	2.2564E−01	–	0.4343
	$40 \times 40 \times 2$	3.5019E−01	0.69	1.3571E−01	0.73	0.6551
	$80 \times 80 \times 2$	2.0042E−01	0.81	7.5993E−02	0.84	0.8059
	$160 \times 160 \times 2$	1.1038E−01	0.86	4.0681E−02	0.90	0.9050
MLP-u1	$20 \times 20 \times 2$	1.7335E−01	–	3.8142E−02	–	0.8191
	$40 \times 40 \times 2$	6.4863E−02	1.42	8.6631E−02	2.14	0.9334
	$80 \times 80 \times 2$	2.3301E−02	1.48	1.9312E−03	2.17	0.9763
	$160 \times 160 \times 2$	8.2233E−03	1.50	4.4283E−04	2.12	0.9917
MLP-u2	$20 \times 20 \times 2$	2.4069E−01	–	5.4225E−02	–	0.7530
	$40 \times 40 \times 2$	1.0045E−01	1.26	1.4353E−02	1.92	0.8987
	$80 \times 80 \times 2$	3.9859E−02	1.33	3.3792E−03	2.09	0.9601
	$160 \times 160 \times 2$	1.5406E−03	1.37	8.3178E−04	2.02	0.9846
Unlimited (least-square)	$20 \times 20 \times 2$	5.9716E−02	–	2.51297E−02	–	0.9760
	$40 \times 40 \times 2$	1.4469E−03	2.05	6.1312E−03	2.04	0.9969
	$80 \times 80 \times 2$	3.5303E−03	2.04	1.5200E−03	2.01	0.9996
	$160 \times 160 \times 2$	8.7445E−04	2.01	3.7912E−04	2.00	0.9999

4.2. Solid body rotation

To assess the behavior of spatial discretization scheme for non-uniform scalar flow field, the following rotational flow field is considered

$$q_t + \mathbf{a} \cdot \nabla q = 0, \quad \mathbf{a} = (-(y - 0.5), (x - 0.5)). \tag{55}$$

The initial profile consists of smooth hump, cone and slotted cylinder [45]. Each shape is located within the circle of radius $r_0 = 0.15$, whose center is (x_0, y_0). Other region is initialized as zero.

Hump:

$$q_0(x, y) = \frac{1}{4}(1 + cos(\pi \min(r(x, y), 1))), \tag{56}$$

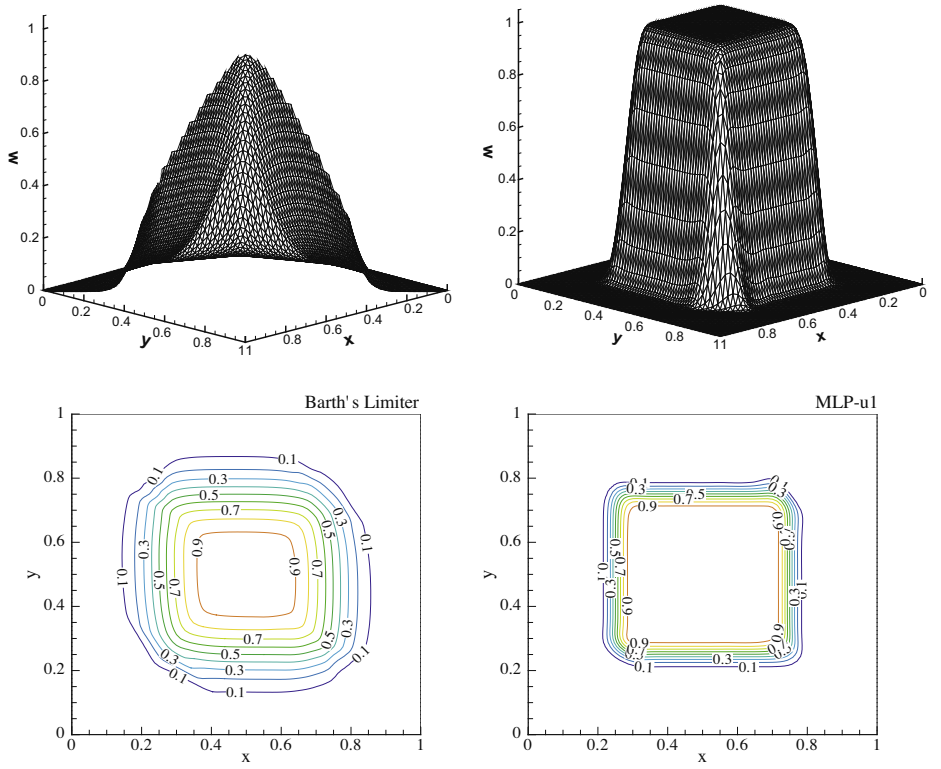

Cone:

$$q_0(x,y) = 1 - r(x,y), \tag{57}$$

Slotted cylinder:

$$q_0(x,y) = \begin{cases} 1 & \text{if } |x - x_0| < 0.25 \text{ or } y > 0.85, \\ 0 & \text{otherwise}, \end{cases} \tag{58}$$

where $r(x,y) = \frac{1}{r_0}\sqrt{(x-x_0)^2 + (y-y_0)^2}$. The center of hump, cone and cylinder is $(0.25, 0.5), (0.5, 0.25), (0.5, 0.75)$, respectively. Computational domain is $[0,1] \times [0,1]$. The upwind scheme is used as a numerical flux and the third-order TVD Runge–Kutta time integration scheme is applied.

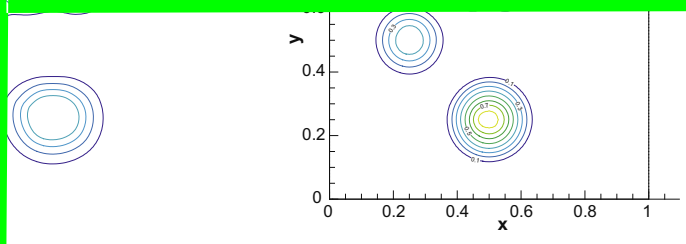

ter one revolution ($t = 2\pi$) with $100 \times 100 \times 2$ type C grid. The result by MLP-u1 limiter urately without unwanted oscillations near discontinuities.

or high-resolution schemes, double Mach reflection is considered [46]. The whole com-ll is located at the bottom of the computational domain beginning at $x = 1/6$. Initially, a ocated at $(x = 1/6, y = 0)$, inclined 60° with respect to the x-axis. Lax–Friedrichs scheme putation is carried out until $t = 0.2$.

ensity contours computed on triangular meshes whose height h is $1/240, 1/480$, respec-e detailed resolution for shock discontinuity as well as flow structure below the Mach around the Mach stem, which shows the accuracy improvement by the MLP limiting.

p

for high-resolution schemes [46]. The problem begins with a uniform Mach 3 flow in e is 3 length unit long and 1 length unit high. The step is 0.2 length unit high, located of the tunnel. Reflective boundary condition is applied along the wall of the tunnel, extrapolation conditions are applied at the entrance and the exit. Around the expansion t any special treatment, as in Ref. [30]. Lax–Friedrich scheme is applied as a numerical

s computed on triangular grids of $h = 1/80, 1/160$ at $t = 4$. Both limiters work well, but better resolution of the slip line from the shock triple point.

erical scheme in multi-dimensional flows without shock waves and turbulence, inviscid Since the flowfield is inviscid, the exact solution is just the passive advection of the ini-

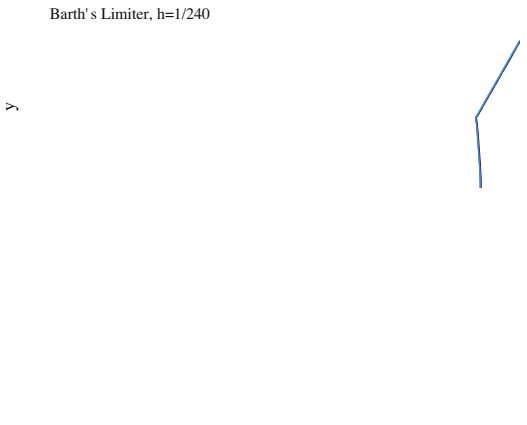

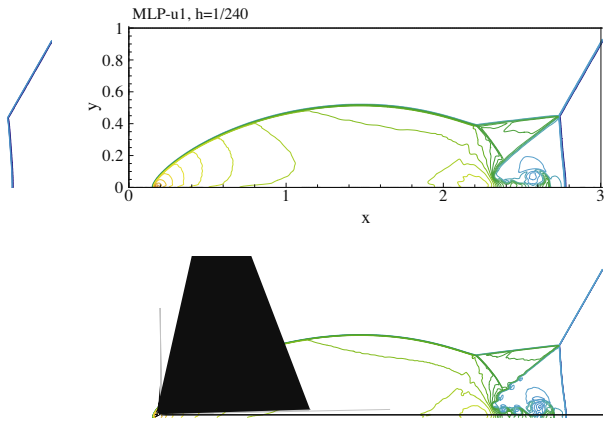

tial vortex with a mean flow. The free stream condition is $\rho_\infty = 1,\ p_\infty = 1$ and $(u_\infty, v_\infty) = (0,0)$. Perturbed values are given by

$$(\delta u, \delta v) = \frac{\varepsilon}{2\pi} e^{0.5(1-r^2)(-\bar{y},\bar{x})}, \quad \delta T = -\frac{(\gamma-1)\varepsilon^2}{8\gamma\pi^2} e^{1-r^2}, \quad \delta S = 0. \tag{59}$$

The strength of the vortex is $\varepsilon = 5$. $(\bar{x}, \bar{y}) = (x - x_0, y - y_0)$, where (x_0, y_0) is the coordinate of the vortex center, and $r^2 = \bar{x}^2 + \bar{y}^2$. From $\rho = \rho_\infty + \delta\rho, u = u_\infty + \delta u, v = v_\infty + \delta v, T = T_\infty + \delta T$ and the isentropic relation, other physical variables can be obtained by

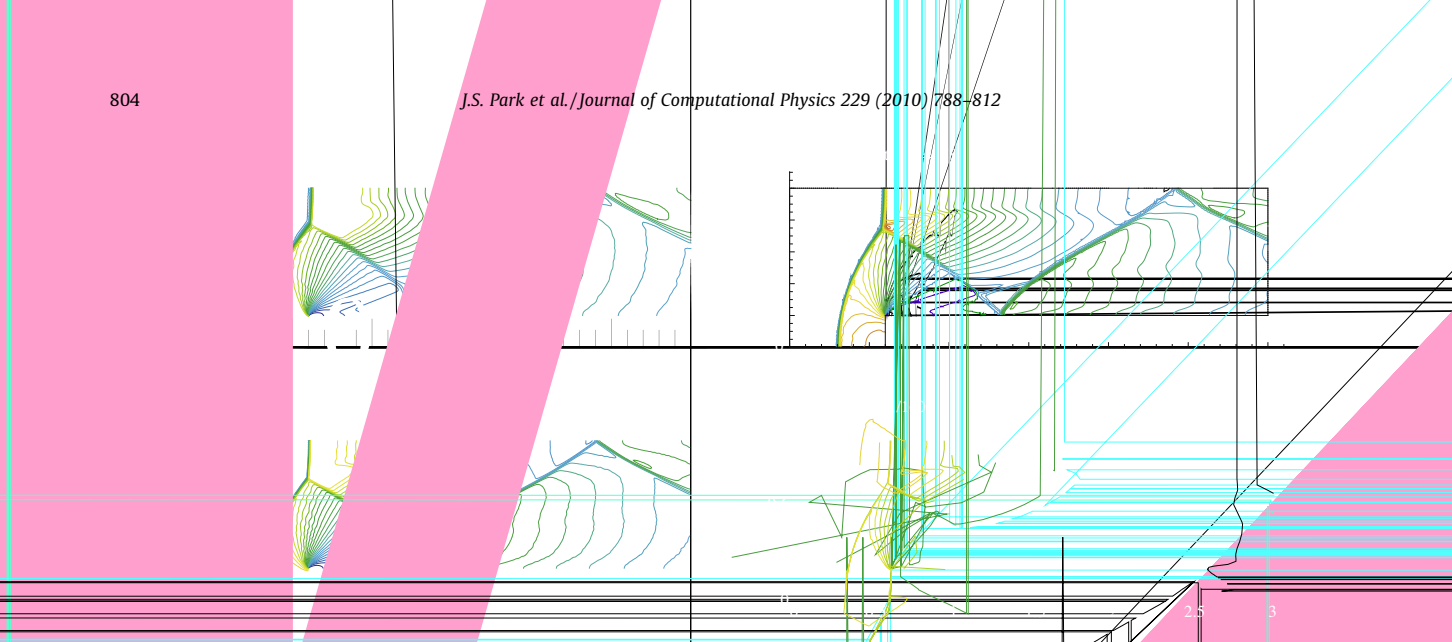

Fig. 15. Comparison of density contours for the Mach 3 wind tunnel with a step. Thirty equally spaced contour lines from $\rho = 0.15$ to $\rho = 6.5$.

$$^{\gamma-1)} = \left[1 - \frac{(\gamma-1)\epsilon^2}{8\gamma\pi} e^{1-r^2}\right]^{1/(\gamma-1)},$$

$$-\frac{\epsilon}{2\pi} e^{(1-r^2)/2}\bar{y}\Bigg],$$

$$\left[1 + \frac{\epsilon}{2\pi} e^{(1-r^2)/2}\bar{x}\right],$$

$$u^2 + v^2).$$

is $-5 \leqslant x \leqslant 5$ and $-5 \leqslant y \leqslant 5$ s applied. Triangular meshes
g uniform square elements alon [40] is applied as a numerical

density contours of computed al dissipation of conventional limiter,
gnificantly smeared and dist the initial vortex shape. Fig. 17 shows
density distribution across evious result, it clearly shows the low-dis-
stic of the MLP limiting. refinement study at time $t = 2$, which dem-
anced accuracy of the

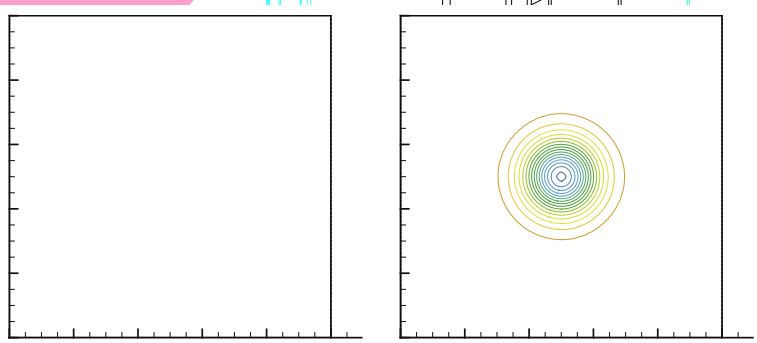

Fig. 16. Density contours of vortex at initial state and $t = 50$.

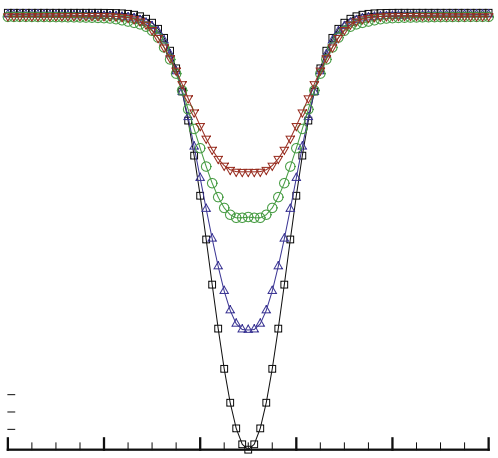

4.6. Shock tube problems

This test is to examine the capability to resolve various linear and non-linear waves on unstructured grids. Computational domain is $[0,1] \times [0,0.1]$ with a triangulation of 101 vertices in the x-direction and 11 vertices in the y-direction. Four Riemann-type initial conditions are considered

Sod problem:

$$(\rho_L, u_L, v_L, p_L) = (1, 0, 0, 1),$$
$$(\rho_R, u_R, v_R, p_R) = (0.125, 0, 0, 0.1). \tag{60}$$

Harten–Lax problem:

$$(\rho_L, u_L, v_R, p_L) = (0.445, 0.698, 0, 3.528),$$
$$(\rho_R, u_R, v_R, p_R) = (0.5, 0, 0, 0.571). \tag{61}$$

Double strong shock problem:

$$(\rho_L, u_L, v_L, p_L) = (5.9924, 19.5975, 0.0, 460.894),$$
$$(\rho_R, u_R, v_R, p_R) = (5.99242, -6.19633, 0.0, 46.0950). \tag{62}$$

Supersonic expansion problem:

$$(\rho_L, u_L, v_R, p_L) = (1.0, -2.0, 0.0, 0.4),$$
$$(\rho_R, u_R, v_R, p_R) = (1.0, 2.0, 0.0, 0.4). \tag{63}$$

RoeM scheme [41] is used as a numerical flux.

Figs. 18–21 show the density and internal energy distributions for each test case. Overall comparison confirms again the better performance of the MLP limiting. Slight oscillations are observed across the contact discontinuity, but they are nearly eliminated by interpolating characteristic variables. For supersonic expansion test, near vacuum state at the center causes a stability problem in maintaining positive density and/or energy. As in Fig. 21, MLP-u1 is not free from this positivity issue, but MLP-u2 successfully computes such a severe flow condition. MLP-u2 captures expansion waves more accurately at the expense of some accentuation of temperature at the center.

4.7. Double shock reflection

Convergence characteristic for steady state flow including shock waves is examined by computing double shock reflection problem. Mach 2 in-flow blows towards the edge whose deflection angle is 15°. The mesh system is composed of 6194 triangle elements.

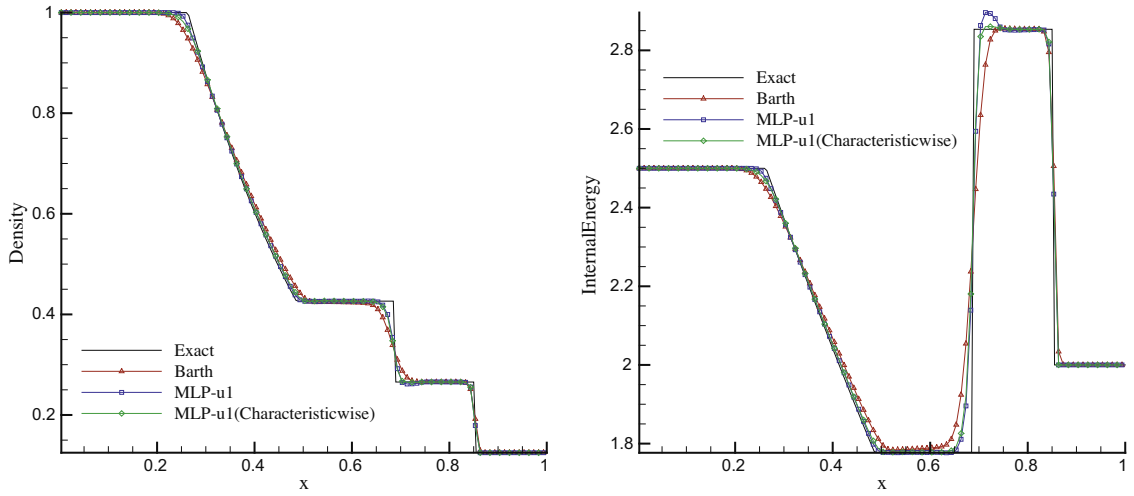

Fig. 18. Density and internal energy distributions along the centerline (Sod problem).

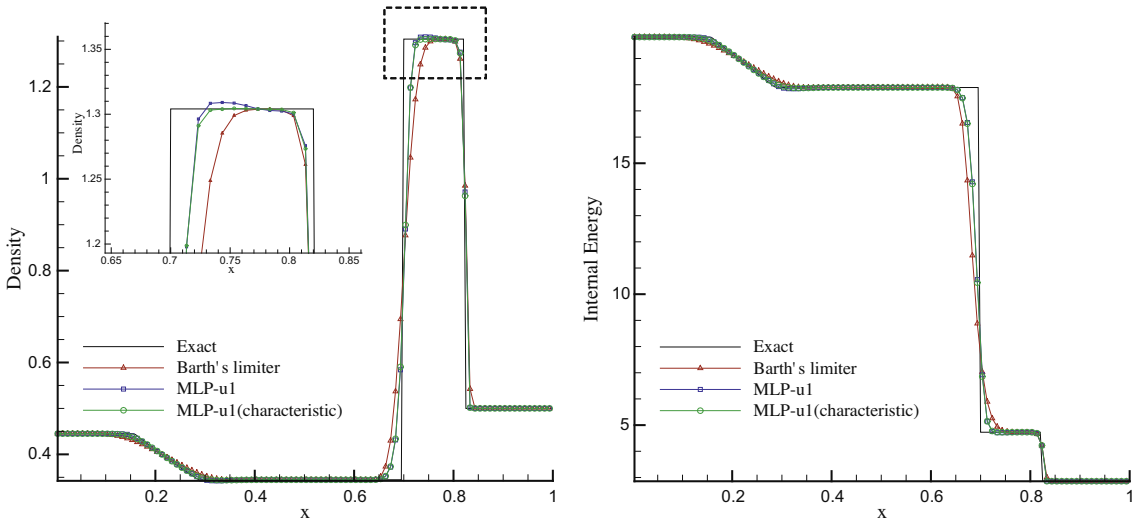

Fig. 19. Density and internal energy distributions along the centerline (Harten–Lax problem).

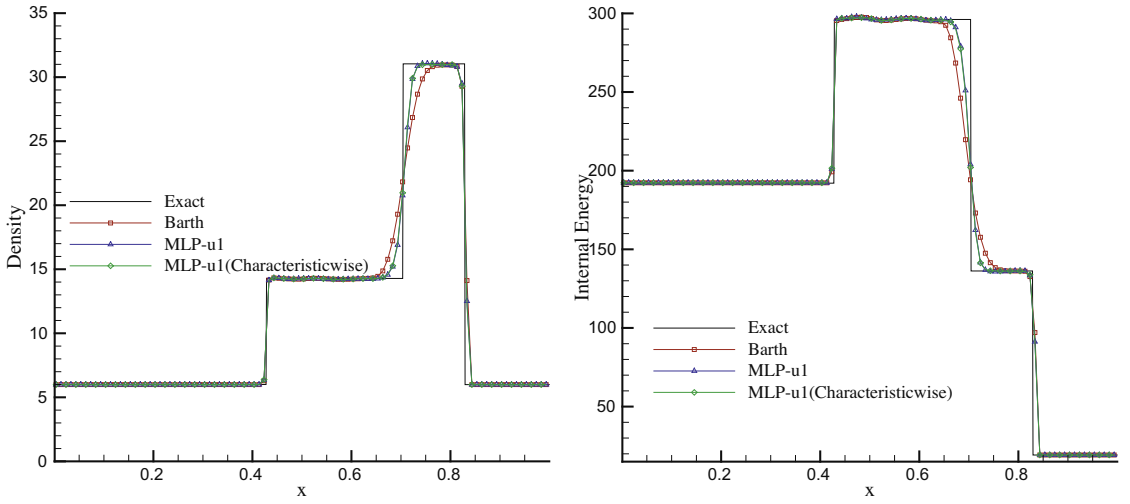

Fig. 20. Density and internal energy distributions along the centerline (double strong shock problem).

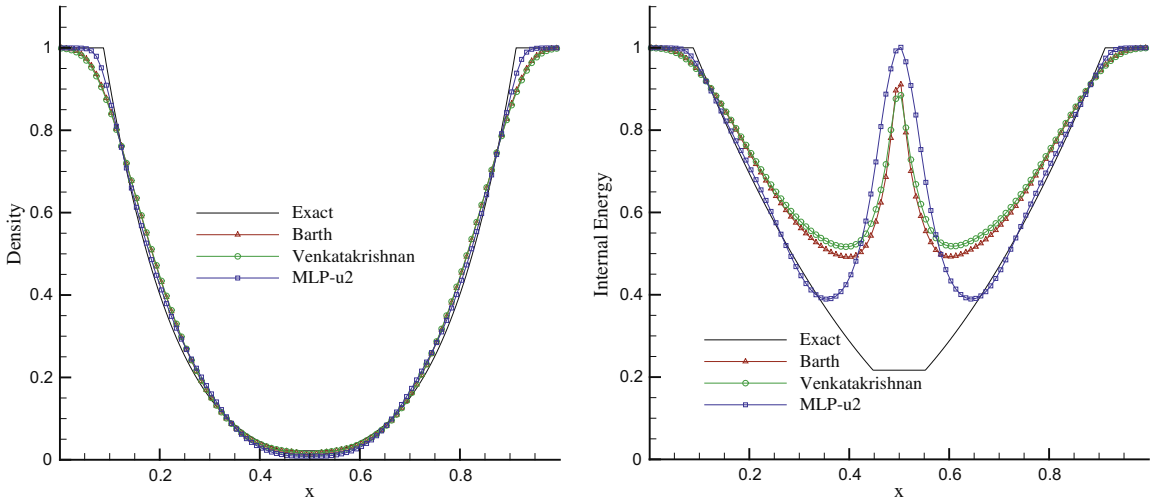

Fig. 21. Density and internal energy distributions along the centerline (supersonic expansion problem).

Fig. 22 compares pressure distributions. All of the computed solutions show little difference and give monotone solutions. However, as shown in Fig. 23, convergence behavior is quite different. While Barth's limiter and non-differentiable MLP-u1 limiter show some trouble to reach a fully converged solution, Venkatakrishinan's limiter and MLP-u2 limiter exhibit an excellent convergence behavior.

4.8. Transonic flows around NACA 0012 airfoil

Due to the coexistence of subsonic and supersonic flows, it may be troublesome to obtain a converged solution for transonic flow. Two cases of transonic flows around the NACA 0012 airfoil are considered: $M = 0.8$ with $\alpha = 1.25^\circ$, and $M = 0.85$ with $\alpha = 1.0^\circ$. The O-type grid whose outer boundary is at 25 chord length is used. The number of surface grid points is 128, and the total number of triangular cells is 10,134 (see Fig. 24).

Fig. 25 shows the convergence history for both cases. Like in case of the double shock reflection, Barth's limiter and non-differentiable MLP-u1 limiter have some trouble, while the solutions by Venkatakrishinan's limiter and MLP-u2 limiter are fully converged. Fig. 26 shows the comparison of the surface pressure coefficient. It is seen that the MLP limiting captures the shock waves more sharply and produces non-oscillatory solutions.

Table 6 summarizes the lift and drag coefficients. The results by the MLP-u limiter agree well with other reference data [47,48]. All of the comparisons demonstrate again the enhanced characteristics of the MLP limiting.

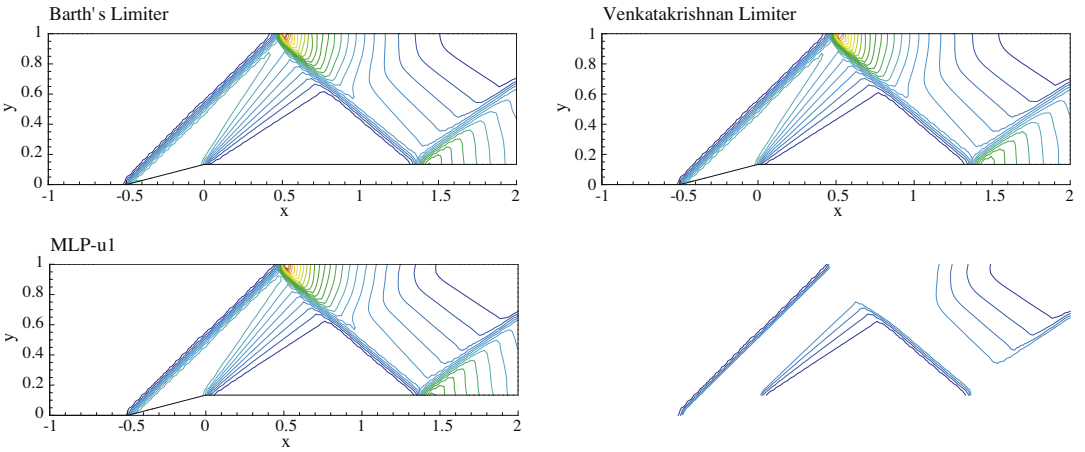

Fig. 23. History (double shock reflection).

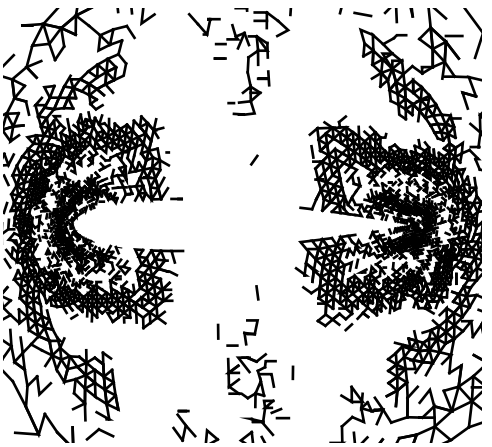

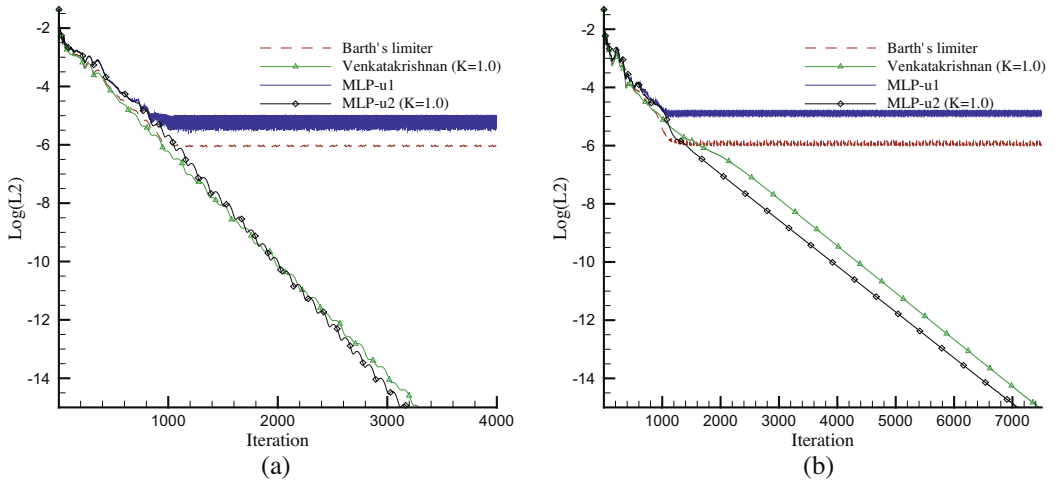

Fig. 25. Error history (NACA 0012 transonic airfoil): (a) $M = 0.8$ and $\alpha = 1.25$ and (b) $M = 0.85$ and $\alpha = 1.0$.

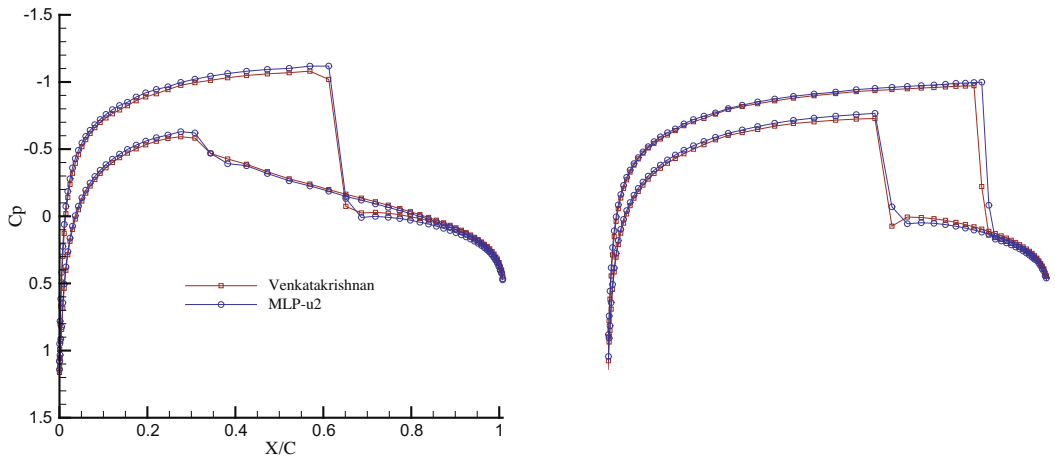

4.9. Viscous shock tube problem

This test case shows viscous flow structure accompanying the interaction between shock wave, boundary layer and vortex. λ-shape shock wave and vortices can be observed by the interaction between the viscous boundary layer at the horizontal wall and the reflective shock wave from the vertical wall [49,33,34].

Computational domain is 1 length unit wide and 1 length unit high, and the diaphragm is located at $x = 0.5$. The initial condition is given as follows

$$(\rho_L, u_L, v_L, p_L) = (120, 0, 0, 120/\gamma), \quad (\rho_R, u_R, v_R, p_R) = (1.2, 0, 0, 1.2/\gamma). \tag{64}$$

The Reynolds number is 200 and the Prandtl number is 0.73. AUSMPW+ scheme is used for inviscid flux calculation and the viscous flux is discretized as in Ref. [50]. The third-order accurate TVD Runge–Kutta time integration method is used with CFL = 0.5.

In Fig. 27, density contours computed by conventional and MLP limiters are compared at $t = 1$. Three different grids ($h = 1/250, 1/350, 1/500$) are considered. The result of the MLP-u1 limiter on coarse grid is similar to that of Barth's limiter on fine grid. Due to excessive numerical diffusion, the shape of vortices obtained by conventional limiter is noticeably smeared (or less rotated). Fig. 28 compares the density distribution along the bottom wall. The result of the MLP-u limiting on coarse grid is closer to the grid-converged solution than that of conventional limiting on fine grid.

Table 7 compares the height of the primary vortex, which, along with its size and rotation angle, is known to be sensitive to the amount of numerical dissipation. From Fig. 27 and Table 7, one can observe again the superior performance of the MLP limiting.

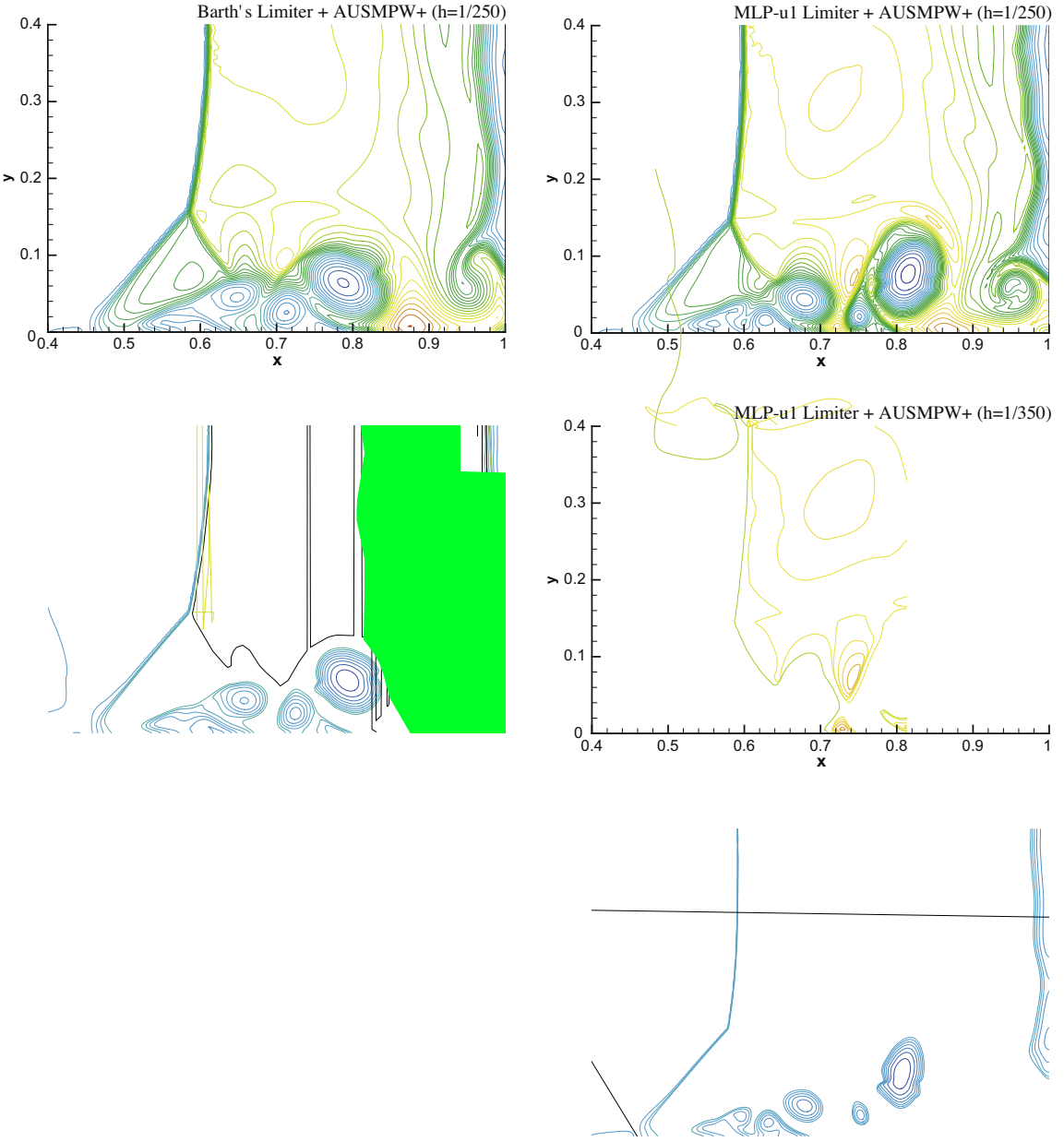

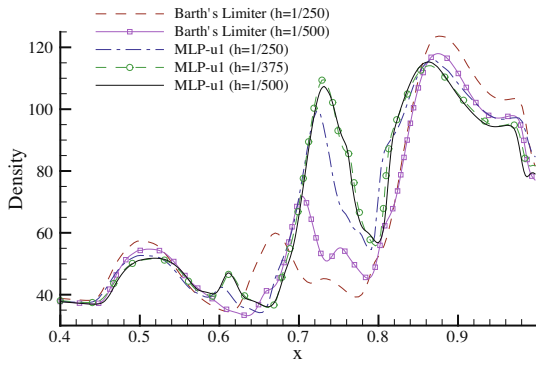

Fig. 28. Comparison of density distributions along the bottom wall.

Table 7
Height of the primary vortex for viscous shock tube.

Limiters	Barth's limiter			MLP-u1		
	(a) 250	(b) 350	(c) 500	(d) 250	(e) 350	(f) 500
Height (H)	0.124	0.135	0.142	0.147	0.161	0.168

5. Conclusion

A new robust and accurate limiting process for multi-dimensional compressible flows on unstructured grids is presented. The proposed limiting strategy is the outcome of the extension of the MLP condition, which has been originally formulated on structured grids. The unstructured grids version of the MLP condition controls physical values at vertex, where local extrema appear in the linearly distributed flow field, by exploiting all of the neighboring cell-centered values. Consequently, the limiting stencil becomes optimally compact and wide enough to accurately capture multi-dimensional flow physics. Furthermore, the MLP condition satisfies the maximum principle, and the stencil for the maximum principle is the same as the stencil for limiting.

Various numerical test cases clearly show the distinguished characteristics of the MLP-u limiter. By maintaining the multi-dimensional monotonicity, numerical accuracy and robustness are significantly improved for linear and non-linear hyperbolic conservation laws. Combined with an advanced flux function, the MLP limiting is expected to accurately capture multi-dimensional flow physics with a reasonable numbers of grid points.

Acknowledgments

The authors appreciate the financial supports provided by NSL (National Space Lab.) program through the National Research Foundation of Korea funded by the Ministry of Education, Science and Technology (Grant 20090091724), the second stage of the Brain Korea 21 Project for Mechanical and Aerospace Engineering Research at Seoul National University, and by Agency for Defense Development. The authors appreciate referees for valuable comments and suggestions.

References

[1] J. Vassberg, E. Tinoco, M. Mani, O. Brodersen, B. Eisfeld, R. Wahls, J. Morrison, T. Zickuhr, K. Laflin, D. Mavriplis, Abridged summary of the third AIAA computational fluid dynamics drag prediction workshop, J. Aircraft 45 (3) (2008) 781–798.
[2] R.T. Biedron, E.M. Lee-Rausch, Rotor airloads prediction using unstructured meshes and loose CFD/CSD coupling, in: Proceedings of the 26th AIAA Applied Aerodynamic Conference, Honolulu, Hawaii, Paper AIAA 2008-7341, 2008.
[3] V.N. Vatsa, M.D. Sanetrik, E.B. Parlette, Development of a Flexible and Efficient Multigrid-based Multi-block Flow Solver, Paper AIAA 93-0677, 1993.
[4] J.L. Steger, F.C. Dougherty, J.A. Benek, A Chimera Grid Scheme, Advanceds in Grid Gerneration, FED 5, ASME Edited, NY, 1983, pp. 59–69.
[5] V. Venkatakrishnan, Perspective on unstructured grid flow solver, AIAA J. 34 (3) (1996) 533–547.
[6] D.J. Mavriplis, Unstructured mesh discretizations and solvers for computational aerodynamics, in: Proceedings of the 18th AIAA Computational Fluid Dynamics Conference, Miami, FL, Paper AIAA 2007-3955, 2007.
[7] H. Luo, J.D. Baum, R. Löhner, High-Reynolds number viscous flow computations using an unstructured-grid method, J. Aircraft 42 (2) (2005) 483–492.
[8] Jing Shi, Yong-Tao Zhang, Chi-Wang Shu, Resolution of high order WENO schemes for complicated flow structures, J. Comput. Phys. 186 (2003) 690–696.
[9] A. Harten, High-resolution schemes for hyperbolic conservation laws, J. Comput. Phys. 49 (1983) 357–393.
[10] P.K. Sweby, High-resolution schemes using flux limiters for hyperbolic conservation laws, SIAM J. Numer. Anal. 21 (5) (1984) 995–1011.
[11] C.W. Shu, TVB uniformly high-order schemes for conservation laws, Math. Comput. 49 (179) (1987) 105–121.
[12] C.W. Shu, S. Osher, Efficient implementation of essentially non-oscillatory shock-capturing schemes, J. Comput. Phys. 77 (1988) 439–471.
[13] X.D. Liu, S. Osher, T. Chan, Weighted essentially non-oscillatory scheme, J. Comput. Phys. 115 (1994) 200–212.

[14] A. Suresh, H.T. Huynh, Accurate monotonicity-preserving schemes with Runge–Kutta time stepping, J. Comput. Phys. 136 (1997) 83–99.
[15] H.C. Yee, N.D. Sandham, M.J. Djomehri, Low-dissipative high-order shock-capturing methods using characteristic-based filters, J. Comput. Phys. 150 (1999) 199–238.
[16] Eric Garnier, Pierre Sagaut, Michel Deville, A class of explicit ENO filters with application to unsteady flows, J. Comput. Phys. 170 (2001) 184–204.
[17] J.B. Goodman, R.J. LeVeque, On the accuracy of stable schemes for 2D scalar conservation laws, Math. Comput. 45 (1985) 15–21.
[18] F. Fezoui, Résolution des équations d'Euler par un schéma de Van Leer en éléments finis, INRIA RR-0358, 1985.
[19] L. Fezoui, B. Stoufflet, A class of implicit upwind schemes for Euler simulations with unstructured meshes, J. Comput. Phys. 84 (1989) 174–206.
[20] T.J. Barth, D. Jespersen, The design and application of upwind schemes on unstructured meshes, in: Proceedings of the 27th AIAA Aerospace Sciences Meeting, Reno, NV, Paper AIAA 89-0366, 1989.
[21] J.A. Desideri, A. Dervieux, Compressible Flow Solvers Using Unstructured Grids, INRIA RR-1732, 1992.
[22] A. Jameson, Analysis and design of numerical schemes for gas dynamics 1: artificial diffusion, upwind biasing, limiters and their effect on accuracy and multigrid convergence, Int. J. Comp. Fluid Dyn. 4 (1995) 171–218.
[23] S.P. Spekreijse, Multigrid solution of monotone second order discretizations of hypersonic conservations laws, Math. Comput. 49 (1987) 135–155.
[24] V. Venkatakrishnan, Convergence to steady state solutions of the Euler equations on unstructured grids with limiters, J. Comput. Phys. 118 (1995) 120–130.
[25] P. Batten, C. Lambert, D.M. Causon, Positively conservative high-resolution convection schemes for unstructured elements, Int. J. Numer. Eng. 39 (1996) 1821–1838.
[26] M.E. Hubbard, Multidimensional slope limiters for MUSCL-type finite volume schemes on unstructured grids, J. Comput. Phys. 155 (1999) 54–74.
[27] T.J. Barth, P.O. Frederickson, Higher order solution of the Euler equations on unstructured grids using quadratic reconstruction, in: Proceedings of the 28th AIAA Aerospace Sciences Meeting, Reno, NV, Paper AIAA 90-0013, 1990.
[28] C. Hu, C.W. Shu, Weighted Essentially Non-oscillatory Schemes on Triangular Meshes, ICASE Report 98-32, 1998, pp. 199–224.
[29] C. Ollivier-Gooch, M.V. Altena, A high-order-accurate unstructured mesh finite-volume scheme for the advection–diffusion equation, J. Comput. Phys. 181 (2002) 729–752.
[30] B. Cockburn, C.W. Shu, The Runge–Kutta discontinuous Galerkin method for conservation laws V: multidimensional systems, J. Comput. Phys. 141 (1998) 199–224.
[31] Z.J. Wang, Spectral (finite) volume method for conservation laws on unstructured grids: basic formulation, J. Comput. Phys. 178 (2002) 210–251.
[32] Z.J. Wang, Y. Liu, G. May, A. Jameson, Spectral difference method for unstructured grids II: extension to the Euler equations, J. Sci. Comput. 32 (1) (2007) 45–70.
[33] K.H. Kim, C. Kim, Accurate, efficient and monotonic numerical methods for multi-dimensional compressible flows Part II: multi-dimensional limiting process, J. Comput. Phys. 208 (2005) 570–615.
[34] S.-H. Yoon, C. Kim, K.H. Kim, Multi-dimensional limiting process for three-dimensional flow physics analyses, J. Comput. Phys. 227 (2008) 6001–6043.
[35] T.J. Barth, Numerical Methods and Error Estimation for Conservation Laws on Structured and Unstructured Meshes, VKI Computational Fluid Dynamics Lecture Series, 2003.
[36] N.T. Frink, Upwind schemes for solving the euler equations on unstructured tetrahedral meshes, AIAA J. 30 (1) (1991) 70–77.
[37] D.J. Mavriplis, Revisiting the least-squares procedures for gradient reconstruction on unstructured meshs, in: Proceedings of the 16th AIAA Computational Fluid Dynamics Conference, Orlando, FL, Paper AIAA 2003-3986, 2003.
[38] B. van Leer, Toward the ultimate conservative difference scheme, J. Comput. Phys. 32 (1979) 101–136.
[39] X.D. Liu, A maximum principle satisfying modification of triangle based adaptive stencils for the solution of scalar hyperbolic conservation Laws, SIAM J. Numer. Anal. 39 (1993) 703–716.
[40] P.L. Roe, Approximate Riemann solvers, parameter vectors, and difference schemes, J. Comput. Phys. 43 (1981) 357–372.
[41] S. Kim, C. Kim, O.H. Rho, S.K. Hong, Cures for the shock instability: development of a shock-stable Roe scheme, J. Comput. Phys. 185 (2003) 342–374.
[42] K.H. Kim, C. Kim, O.H. Rho, Methods for the accurate computations of hypersonic flows, part I: AUSMPW+ scheme, J. Comput. Phys. 174 (2001) 38–80.
[43] C.W. Shu, Total-variation-diminishing time discretization, SIAM J. Sci. Stat. Comput. 9 (6) (1988) 1073–1084.
[44] J.T. Batina, Implicit upwind solution algorithms for three-dimensional unstructured meshes, AIAA J. 31 (5) (1993) 801–805.
[45] R.J. Leveque, High-resolution conservative algorithms for advection in incompressible flow, SIAM J. Numer. Anal. 33 (1996) 627–665.
[46] P. Woodward, P. Colella, The numerical simulation of two-dimensional fluid flow with strong shocks, J. Comput. Phys. 54 (1984) 115–173.
[47] AGARD AR-211, Test Cases for Inviscid Flow Field, AGARD, 1985.
[48] J.C. Vassberg, A. Jameson, In pursuit of grid convergence, part I: two-dimensional Euler equations, in: Proceedings of the 27th AIAA Applied Aerodynamics Conference, San Antonio, TX, Paper AIAA 2009-4114, 2009.
[49] V. Daru, C. Tenaud, Evaluation of TVD high-resolution schemes for unsteady viscous shocked flows, Comput. Fluids 30 (2001) 89–113.
[50] N.T. Frink, Tetrahedral unstructured Navier–Stokes method for turbulent flows, AIAA J. 36 (11) (1998) 1975–1982.